Jupiter's X-ray Emission 2007 Part 2: Comparisons with UV and Radio Emissions and In-Situ Solar Wind Measurements

W.R. Dunn, R. Gray, A.D. Wibisono, L. Lamy, C. Louis, S.V. Badman, G. Branduardi-Raymont, R. Elsner, Randy Gladstone, R. Ebert, et al.

▶ **To cite this version:**

W.R. Dunn, R. Gray, A.D. Wibisono, L. Lamy, C. Louis, et al.. Jupiter's X-ray Emission 2007 Part 2: Comparisons with UV and Radio Emissions and In-Situ Solar Wind Measurements. Journal of Geophysical Research Space Physics, 2020, 125 (6), pp.e27222. 10.1029/2019JA027222 . insu-02569228

HAL Id: insu-02569228
https://insu.hal.science/insu-02569228

Submitted on 9 Sep 2020

HAL is a multi-disciplinary open access archive for the deposit and dissemination of scientific research documents, whether they are published or not. The documents may come from teaching and research institutions in France or abroad, or from public or private research centers.

L'archive ouverte pluridisciplinaire **HAL**, est destinée au dépôt et à la diffusion de documents scientifiques de niveau recherche, publiés ou non, émanant des établissements d'enseignement et de recherche français ou étrangers, des laboratoires publics ou privés.

Distributed under a Creative Commons Attribution - NoDerivatives 4.0 International License

JGR Space Physics

RESEARCH ARTICLE
10.1029/2019JA027222

This article is a companion to Dunn et al. (2020), https://doi.org/10.1029/2019JA027219.

Key Points:
- We characterize three types of X-ray aurorae (main oval, ir/regular pulses, and flickering aurorae) and compare with radio, UV, and solar wind data
- Non-Io decametric bursts occurred with UV auroral brightening, and UV and hard X-ray main auroral emission also brightened contemporaneously
- Soft X-ray aurora was best fit by iogenic (S, O) spectral lines except during magnetospheric expansion when solar wind ion lines were needed

Supporting Information:
- Supporting Information S1

Correspondence to:
W. R. Dunn,
w.dunn@ucl.ac.uk

Citation:
Dunn, W. R., Gray, R., Wibisono, A. D., Lamy, L., Louis, C., Badman, S. V., et al. (2020). Comparisons between Jupiter's X-ray, UV and radio emissions and in-situ solar wind measurements during 2007. *Journal of Geophysical Research: Space Physics*, *125*, e2019JA027222. https://doi.org/10.1029/2019JA027222

Received 31 JUL 2019
Accepted 31 MAR 2020
Accepted article online 7 APR 2020

©2020. The Authors.
This is an open access article under the terms of the Creative Commons Attribution License, which permits use, distribution and reproduction in any medium, provided the original work is properly cited.

Comparisons Between Jupiter's X-ray, UV and Radio Emissions and In-Situ Solar Wind Measurements During 2007

W. R. Dunn[1,2,3], R. Gray[4], A. D. Wibisono[1,2], L. Lamy[5,6], C. Louis[6,7], S. V. Badman[4], G. Branduardi-Raymont[1,2], R. Elsner[8], G. R. Gladstone[9], R. Ebert[9,10], P. Ford[11], A. Foster[3], C. Tao[12], L. C. Ray[4], Z. Yao[13], I. J. Rae[1], E. J. Bunce[14], P. Rodriguez[15], C. M. Jackman[16,17], G. Nicolaou[1], J. Clarke[18], J. Nichols[14], H. Elliott[6], and R. Kraft[3]

[1]Mullard Space Science Laboratory, Department of Space and Climate Physics, University College London, Dorking, UK, [2]The Centre for Planetary Science at UCL/Birkbeck, London, UK, [3]Harvard-Smithsonian Center for Astrophysics, Smithsonian Astrophysical Observatory, Cambridge, MA, USA, [4]Department of Physics, Lancaster University, Lancaster, UK, [5]LESIA, Observatoire de Paris, PSL Research University, CNRS, Sorbonne Universités, UPMC Univ. Paris 06, Univ. Paris Diderot, Sorbonne Paris Cité, Meudon, France, [6]USN, Observatoire de Paris, CNRS, PSL, UO/OSUC, Nançay, France, [7]IRAP, Université de Toulouse, CNRS, CNES, UPS, Toulouse, France, [8]ZP12, NASA Marshall Space Flight Center, Huntsville, AL, USA, [9]Space Science and Engineering Division, South West Research Institute, San Antonio, TX, USA, [10]Department of Physics and Astronomy, The University of Texas at San Antonio, San Antonio, TX, USA, [11]Kavli Institute of Astrophysics and Space Research, MIT, Cambridge, MA, USA, [12]National Institute of Information and Communications Technology, Koganei, Japan, [13]Laboratoire de Physique Atmospherique et Planetaire, Université de Liege, Liege, Belgium, [14]Department of Physics and Astronomy, University of Leicester, Leicester, UK, [15]European Space Astronomy Centre, Madrid, Spain, [16]Department of Physics and Astronomy, University of Southampton, Southampton, UK, [17]Dublin Institute for Advanced Studies, Dublin, Ireland, [18]Center for Space Physics, Boston University, Boston, MA, USA

Abstract We compare Chandra and XMM-Newton X-ray observations of Jupiter during 2007 with a rich multi-instrument data set including upstream in situ solar wind measurements from the New Horizons spacecraft, radio emissions from the Nançay Decametric Array and Wind/Waves, and ultraviolet (UV) observations from the Hubble Space Telescope. New Horizons data revealed two corotating interaction regions (CIRs) impacted Jupiter during these observations. Non-Io decametric bursts and UV emissions brightened together and varied in phase with the CIRs. We characterize three types of X-ray aurorae: hard X-ray bremsstrahlung main emission, pulsed/flared soft X-ray emissions, and a newly identified dim flickering (varying on short time scales, but quasi-continuously present) aurora. For most observations, the X-ray aurorae were dominated by pulsed/flaring emissions, with ion spectral lines that were best fit by iogenic plasma. However, the brightest X-ray aurora was coincident with a magnetosphere expansion. For this observation, the aurorae were produced by both flickering emission and erratic pulses/flares. Auroral spectral models for this observation required the addition of solar wind ions to attain good fits, suggesting solar wind entry into the outer magnetosphere or directly into the pole for this particularly bright observation. X-ray bremsstrahlung from high energy electrons was only bright for one observation, which was during a forward shock. This bremsstrahlung was spatially coincident with bright UV main emission (power > 1 TW) and X-ray ion spectral line dusk emission, suggesting closening of upward and downward current systems during the shock. Otherwise, the bremsstrahlung was dim, and UV main emission power was also lower (<700 GW), suggesting their power scaled together.

1. Introduction

Jupiter produces diverse and dynamic multiwaveband auroral emissions. Radio, infrared, visible, ultraviolet (UV), and X-ray auroral emissions have all been observed from the planet (e.g., Badman et al., 2015, and Bagenal et al., 2014, and references therein). While auroral emissions from the footprints of Jovian satellites (Bhattacharyya et al., 2018; Bonfond et al., 2009, 2013; Hess et al., 2010, 2011; Jia et al., 2010; Kivelson, 2004; Saur et al., 2004; Szalay et al., 2018; Zarka, 1998) and from low-latitude injection events (Kimura et al., 2015;

Mauk et al., 2002) are observed in many wavebands, they are yet to be observed in the X-rays, so we focus on Jupiter's auroral main emission and the regions poleward of this.

Jupiter's dominant aurora is its "main emission," which is a near-continuous auroral emission that occurs near the footprints of Ganymede and Callisto (e.g., Grodent et al., 2008). This bright emission is produced by an upward current system that transfers angular momentum from the planet to plasma in the middle magnetosphere (15–40 Jupiter radii [R_J]) in order to enforce corotation (e.g., Cowley & Bunce, 2001; Hill, 2001). This upward current system leads electrons to precipitate into Jupiter's upper atmosphere producing radio, infrared, UV, and hard X-ray bremsstrahlung emissions (summarized in, e.g., Badman et al., 2015; Bagenal et al., 2014, and references therein).

Poleward of Jupiter's main emission (mapping beyond 40 R_J), there are a diverse variety of UV auroral flares, swirls, arcs, and dark regions (e.g., Grodent, 2015, and references therein). The process that produces most of these is yet to be confirmed. On the dawnside of the polar aurorae, there is the dark polar region that is seemingly absent of emission but features occasional spots of emission that may relate to reconnection return flows (Gray et al., 2016; Radioti et al., 2011). In the center of the polar region, there is the "swirl region" from which intermittent pulses of emission are observed, whether or not this is Jupiter's open field line region is a topic of debate (e.g., Cowley et al., 2003, 2008; Delamere & Bagenal, 2010; McComas & Bagenal, 2007; Stallard et al., 2003; Vogt et al., 2015). Streams of MeV electrons are accelerated away from Jupiter in the swirl region suggesting a source of high acceleration close to the planet (Paranicas et al., 2018), but a connection between these MeV electrons and auroral emissions has not yet been identified. Occasionally, long thin auroral arcs or "filaments" bound this region centered on noon and may relate to high latitude reconnection (Nichols et al., 2009a). In the polar regions between noon and dusk, UV and X-ray auroral pulses (or "flares") are observed (Bonfond et al., 2011, 2016; Branduardi-Raymont et al., 2008; Elsner et al., 2005; Gladstone et al., 2002; Nichols, Badman, et al., 2017).

UV emissions are caused by electron collisions that excite hydrogen in Jupiter's atmosphere. In contrast, the soft X-ray pulses are dominated by spectral lines from the collision of highly charged ions (e.g., $O^{6+,7+}$) with the atmosphere (e.g., Branduardi-Raymont et al., 2004, 2007). These lines are produced when ions collide with atmospheric neutrals and charge exchange to take an electron from a neutral and consequently emit an X-ray photon (Cravens et al., 1995). If the precipitating ions are of a magnetospheric origin, then they will be only singly or doubly charged (e.g., $O^{+,2+}$) and must therefore undergo a series of high energy (>0.5 MeV/u) collisions that strip electrons from them before they are of a sufficiently high charge state (e.g., $O^{6+,7+}$) to produce the observed X-ray spectral lines (Houston et al., 2018, 2020). Clark et al. (2017) have shown that large potential drops do exist over Jupiter's pole, which may provide at least part of the ion acceleration to produce the observed X-rays. Alternatively, solar wind ions already exist in a sufficiently high charge state but would require extremely large currents (~MA) in order to provide large enough ion fluxes for the X-ray spectral lines observed (Cravens et al., 2003).

A variety of processes have been proposed to explain the precipitation of X-ray-producing ions in the polar region including downward current systems in the outer magnetosphere that complete the upward corotation enforcement system (Cravens et al., 2003), dayside reconnection and/or cusp processes (Bunce et al., 2004; Pallier & Prangé, 2001, 2004), Kelvin-Helmholtz instabilities (Dunn et al., 2016, 2017; Kimura et al., 2016), rotation-driven reconnection in the outer magnetosphere (Guo, Yao, Sergis, et al., 2018; Guo, Yao, Wei, et al., 2018; Yao et al., 2017), and/or a combination of wave processes (e.g., Manners et al., 2018). The source for auroral flares near regions mapping to the magnetopause suggests that the emission may be diagnostic of the relationship between Jupiter's magnetosphere and the solar wind.

1.1. Connections Between the Aurora and the Solar Wind

Jupiter's auroral response to changes in solar wind pressure has been studied using a variety of wavebands and theoretical arguments (e.g., Baron et al., 1996; Chané et al., 2017; Cowley & Bunce, 2001; Prangé et al., 1993; Sinclair et al., 2019; Southwood & Kivelson, 2001; Zarka, 1998). Clarke et al. (2009) and Nichols et al. (2009b) showed that the UV main emission brightens and thickens in response to solar wind shocks. Badman et al. (2016) showed that the inverse is also true and that magnetospheric expansion leads the main emission to dim and shift to lower latitudes, through reduced electron density and thermal energy or increased inward (outward) transport of hot (cold) plasma. Nichols, Badman, et al. (2017) also showed that solar wind compressions can trigger pulsing arcs of UV emission in the dusk sector, which may relate to tail reconnection or velocity shears. Kita et al. (2016) have shown that not only does the UV auroral

brightness vary with solar wind conditions but that there is a correlation between the total auroral power and the length of the quiescent interval that preceded the solar wind shock. Grodent et al. (2018) analyzed an extensive Hubble Space Telescope (HST) campaign to identify several classes of auroral behavior of which they characterize one that is driven by external conditions.

Jovian radio emissions can also be triggered by solar wind conditions and can therefore be used as a proxy for compressions/rarefactions (Desch & Barrow, 1984; Dunn et al., 2016; Echer et al., 2010; Gurnett et al., 2002; Hess et al., 2012, 2014; Prangé et al., 2004; Lamy et al., 2012). Hess et al. (2012, 2014) in particular showed that forward and reverse solar wind shocks can be distinguished through differing time frequency morphology of bursts of Jovian non-Io decametric emission, namely, the rise of duskside and dawnside/duskside sources, respectively.

X-ray emissions from Jupiter have also exhibited a solar wind relationship, but this is less well catalogued than for the radio and UV. Branduardi-Raymont et al. (2007) noted that X-ray emissions increased during an interval of pronounced solar activity. Dunn et al. (2016) found significant changes in the spatial, spectral, and temporal trends of Jupiter's aurora between an observation during an Interplanetary Coronal Mass Ejection (ICME) impact and an observation during ICME recovery. Kimura et al. (2016) found correlations between solar wind velocity and the X-ray emissions. In the absence of upstream solar wind measurements, both Dunn et al. (2016) and Kimura et al. (2016) propagated solar wind conditions from measurements at 1 AU to Jupiter at ~5 AU. These propagation models had large timing uncertainties (±10–15 hr in Dunn et al., 2016, and ±48 hr in Kimura et al., 2016), and this may have at least partially lead to the two works contradictory results, in which the former suggests a connection with solar wind density but not velocity and the latter with velocity, but not density. This present study provides a rare opportunity to examine contemporaneous auroral data with solar wind information from an upstream monitor.

1.2. Connections Between Different Auroral Wavebands

Leveraging the UV and X-ray wavebands together lets one utilize the high-photon counts observed by HST (typically for ~40 min at a time) in partnership with the longer duration (up to 40 hr) but lower count rate X-ray observations by Chandra or XMM-Newton. A single overlapping observation has produced two important findings: At least some UV and X-ray auroral flares are coincident (within a few 1,000 km) (Elsner et al., 2005), and the UV main emission is coincident with the X-ray electron bremsstrahlung emission (Branduardi-Raymont et al., 2008).

Quasiperiodic flaring has also been observed in the UV polar aurora and main emission with periods of a few to 10 min (Bonfond et al., 2011, 2016; Nichols, Badman, et al., 2017; Nichols, Yeoman, et al., 2017). The 40 min duration of HST observations means regular pulsations with a longer interpulse time than this would be difficult to identify; however, the several hour X-ray observations have detected regular pulses of 8–45 min in ~10 observations (Dunn et al., 2016; Gladstone et al., 2002; Jackman et al., 2018). For most other observations, the X-ray aurora still pulses, but these pulses are more erratic and the poles sometimes behave independently and sometime pulse in tandem (Dunn et al., 2017). Recent observations in the infrared have also revealed emissions poleward of the UV main emission that pulsed on time scales of 10 min (Watanabe et al., 2018).

Periodic radio pulsations also occur with similar characteristic periods to the X-ray pulses and may be produced by electrons streaming away from the planet (MacDowall et al., 1993). Bursts of non-Io decametric radio emission have also been observed to occur contemporaneously with significant brightening of the X-ray aurora (Dunn et al., 2016).

Through February and March 2007, NASA's New Horizons spacecraft was approaching Jupiter. At this time, a series of HST, Chandra, and XMM-Newton observations of Jupiter were conducted, while radio observations by Wind/Waves and the NDA (Nançay Decameter Array) were ongoing. The combination of these campaigns provides a rich multiwaveband data set. In this paper, we utilize these data to explore links between Jovian X-ray emissions, other aurora wavebands, and the solar wind. This is the second in a series of papers that include the Jovian X-ray data from 2007. The first paper (Dunn et al., 2020) reported general trends in the equatorial and auroral X-ray emissions during solar minimum.

In this work, we begin by introducing the February and March 2007 remote observation campaigns (section 2). We then present the New Horizons solar wind measurements (section 3) and the more thoroughly studied UV (section 4) and radio (section 5) wavebands to provide further context for the X-ray

Table 1
Table of Jupiter Observations Dates and Times and Central Meridian Longitude (CML) Ranges During Chandra (CXO), XMM-Newton (XMM), and Hubble Space Telescope (HST) Observations in February and March 2007

Instrument	Date	Time (UT)	DOY	CML (°)	Aurora (N/S)	General SW Conditions
CXO	8 Feb	08:31 - 13:47	39	94–286	N	CIR Day 4
CXO	10-11 Feb	19:54 - 01:21	41–42	88–286	N	Rarefaction
HST	21 Feb	15:21 - 16:04	52	141–167	N	Rarefaction
HST	22 Feb	11:12 - 11:14	53	141–142	N	Rarefaction
HST	23 Feb	08:56 - 09:05	54	209–215	N	CIR Arrival
HST	24 Feb	12:50 - 14:25	55	141–198	N	CIR Day 2
CXO	24–25 Feb	21:24 - 02:17	55–56	90–267	N	CIR Day 2
XMM	24–25 Feb	20:14 - 03:02	55–56	47–294	N	CIR Day 2
HST	26 Feb	15:17 - 15:59	57	171–197	N	CIR Day 3
HST	27 Feb	10:29 - 11:11	58	147–173	N	CIR Day 4/Rarefaction
HST	2 Mar	07:46 - 09:13	61	140–193	N	Rarefaction
HST	3 Mar	04:05 - 05:45	62	157–218	N	Rarefaction
CXO	3 Mar	07:43 - 13:03	62	286–120	S	Rarefaction or CIR Arrival
XMM	3 Mar	07:17 - 14:42	62	271–180	S	Rarefaction or CIR Arrival
HST	4 Mar	10:24 - 11:06	63	177–202	N	CIR Arrival
HST	5 Mar	05:35 - 06:18	64	153–179	N	CIR Day 2
HST	6 Mar	11:01 - 11:05	65	140–143	N	CIR Day 3
CXO	7 Mar	14:19 - 19:08	66	48–223	~N	CIR Day 4/Rarefaction
XMM	7 Mar	12:52 - 20:21	66	356–267	S→N	CIR Day 4/Rarefaction
CXO	8–9 Mar	21:04 - 02:45	67–68	83–290	N	Rarefaction
XMM	8–9 Mar	19:50 - 02:20	67–68	39–275	N	Rarefaction
HST	9 Mar	09:10 - 10:38	68	164–218	N	Rarefaction
HST	10 Mar	04:29 - 04: 39	69	146–151	N	Rarefaction

Note. Figures 1 and 2 are interpreted to provide instances of solar wind rarefactions and compressions from corotating interaction regions (CIR) for each observation.

emissions. Having built an understanding of the conditions, we present the variation in X-ray spectra (section 6.2), spatial morphology (section 6.3), and temporal signatures (section 6.4) from observation to observation. We close by connecting the different X-ray auroral behaviors with the solar wind and multi-waveband observations (section 7).

2. February and March 2007 Remote Observations of Jupiter

2.1. Chandra and XMM-Newton X-Ray Campaign

Through February and March 2007, a series of Jupiter X-ray observations were conducted with Chandra's ACIS instrument and with the XMM-Newton Observatory. The X-ray observations were shorter than other Jovian X-ray campaigns lasting ~0.5 Jupiter rotations each. Jupiter's subobserver latitude was −3.31° , so the northern geographic pole was slightly obscured. The observation times and associated longitude ranges are listed in Table 1. Unlike Earth's aurora, Jupiter's main auroral emission is fixed in planetary (System III [S3]) longitude and thus rotates with the planet. The dipole tilt means that the longitude locations are different for each pole. For the north, the aurorae are more strongly offset from the spin axis and mostly situated between ~140° and 270° S3 longitude and above 55° latitude. The southern aurorae are more closely aligned to the spin axis but still feature an offset with a viewing preference from ~300° to 120° longitude and above 60° latitude. Table 1 therefore shows that the observations on 8, 10–11, and 24–25 February and 8–9 March provided coverage of the northern aurora, while 3 March covered the southern aurora (and is discussed in Dunn et al., 2017) and 7 March covered a transition between the two. For all Chandra observations, the combination of red leak through the ACIS Optical Blocking Filter and contaminant buildup had to be accounted for in the manner described in Elsner et al. (2005) and Dunn et al. (2017).

Table 2
Table of Detected Non-Io Decametric Emissions From Jupiter by the NDA and WIND/WAV Instruments from 27 January to 10 March 2007

Date - Time	Vertex Early/Late	Instrument (NDA/WAV)
27 Jan 08:00 - 08:07	Late	NDA
27 Jan 08:25 - 08:32	Late	NDA
27 Jan 09:30 - 12:00	Late	WAV
27 Jan 21:00 - 23:55	Late	WAV
28 Jan 04:42 - 05:03	Late	NDA
28 Jan 17:00 - 18:00	Late	WAV
29 Jan 14:30 - 15:45	Late	WAV
30 Jan 11:00 - 12:00	Late	WAV
31 Jan 03:00 - 04:00	Early	WAV
31 Jan 17:00 - 18:00	Late	WAV
4 Feb 21:30 - 22:00	Early	WAV
5 Feb 09:00 - 10:00	Late	WAV
5 Feb 15:30 - 16:30	Late	WAV
5 Feb 19:00 - 20:00	Late	WAV
7 Feb 05:11 - 05:35	Late	NDA
8 Feb 03:00 - 04:00	Late	WAV
8 Feb 13:00 - 14:00	Early	WAV
9 Feb 02:50 - 03:10	Early	WAV
9 Feb 06:00 - 07:00	Late	WAV
9 Feb 19:00 - 20:00	Late	WAV
10 Feb 04:59 - 05:24	Late	NDA
13 Feb 22:30 - 23:30	Late	WAV
14 Feb 08:30 - 09:30	Late	WAV
14 Feb 18:00 - 19:00	Early	WAV
23 Feb 05:30 - 07:00	Late	WAV
5 Mar 03:09 - 03:22	Late	NDA
10 Mar 05:30 - 07:30	Early	WAV
10 Mar 09:30 - 11:30	Late	WAV

Note. NDA measurements are from the Marques et al. (2017) catalogue of decametric emissions. The early or late morphology from Hess et al. (2014) for each non-Io decametric arc is listed.

2.2. UV Observation Campaign

From 20 February to 10 March 2007 (inclusive), there was an extensive HST UV observing campaign with the Advanced Camera for Surveys Solar Blind Channel. This consisted of 907 (580) UV images of the northern (southern) aurora, taken in groups of 15 images spanning <1 hr, with most exposures lasting ~100 s (discussed in detail in Clarke et al., 2009; Nichols et al., 2009b; and Stallard et al., 2016). Table 1 shows the UV observations contemporaneous to the X-ray observations.

2.3. Radio Observation Campaign

Since 1977, the NDA has observed Jupiter radio emissions for ~8 hr per day between 10 and 40 MHz (Boischot et al., 1980; Lamy et al., 2017; Lecacheux, 2000; www.obs-nancay.fr). The NDA measurements obtained with its routine receiver display a good time frequency resolution (1 s × 75 kHz) while its polarization capability enables one to disentangle the hemisphere of origin of decametric extraordinary mode emission (RH or LH polarized when emitted from the northern or southern hemisphere, respectively). These capabilities allowed Marques et al. (2017) to conduct a statistical analysis of radio emissions from Jupiter and generate a catalogue of these emissions. We list the non-Io arcs from their catalogue in Table 2.

The WIND spacecraft has operated since 1993. Its Waves instrument measures radio emission from a few Hz to 14 MHz (Bougeret et al., 1995) and provides quasi-continuous measurements at moderate time frequency

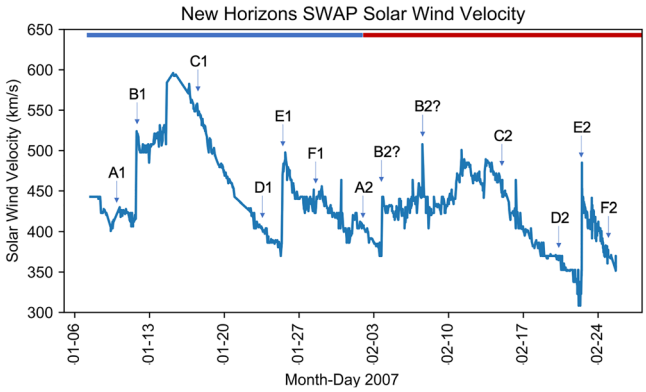

Figure 1. Solar wind velocities upstream of Jupiter as measured by the New Horizons SWAP instrument from 6 January to 26 February 2007 (inclusive). ABC and DEF indicate two distinct corotating interaction regions which impact Jupiter multiple times during this interval. Each interval when they impact Jupiter is indicated by their numbering (e.g., B1 indicates the first arrival of the shock B at Jupiter; E2 indicates the second arrival of shock E). New Horizons passed into Jupiter's magnetosphere on 26 February. Alternating blue and red bars at the top of the plot indicate solar rotations.

resolution (60 s × 50 kHz in this study) so that while it is designed to track solar radio bursts, it is sensitive enough to remotely detect emissions from Jupiter (and other radio sources).

3. New Horizons Solar Wind Measurements

On 26 February 2007, New Horizons entered Jupiter's magnetosphere for a Jupiter flyby. Prior to this, the Solar Wind Around Pluto (SWAP) instrument (McComas et al., 2008) measured the solar wind conditions upstream of Jupiter. From 8 February onwards, there was a propagation time between New Horizons and the Jovian bow shock of between a few hours and 19 hr (depending on the specific solar wind conditions at that time, the magnetosphere extent and the New Horizons-bow shock distance). SWAP is built for the more rarified solar wind conditions near the orbit of Pluto (Bagenal et al., 2016; Elliott et al., 2016, 2018; McComas et al., 2007, 2016) but has been used successfully to study the Jovian magnetotail (Ebert et al., 2010), magnetosheath (Nicolaou et al., 2014), magnetotail boundary layer (Nicolaou et al., 2015), and the solar wind at various locations in the heliosphere (Elliott et al., 2016, 2019). Figure 1 shows the SWAP estimates of the solar wind velocity upstream of Jupiter from 10 January to 26 February 2007. This was during an extended solar minimum, when solar wind structures are expected to be well organized with solar rotation and ICMEs would be rare (e.g., Owens & Forsyth, 2013).

Figure 1 shows several solar wind structures labeled alphabetically. Their recurrence with solar rotation is indicated numerically, so that the structures ABC and DEF recur each solar rotation. A and D indicate slow quiescent solar wind prior to a shock. B and E indicate the arrival of a shock that recurs approximately every solar rotation. C and F show the declines from fast solar wind through to slower solar wind. We interpret the shocks at B and E as corotating interaction regions (CIRs). A CIR occurs where slow solar wind (e.g., A1) is caught up by fast solar wind. The fast wind (e.g., C1) is slowed at the shock (e.g., B1) where the populations meet and the solar wind density increases in this region. These density increases will act to compress Jupiter's magnetosphere. The shocked fast wind then passes New Horizons and SWAP measures fast unshocked solar wind (e.g., C1), which then transitions to slow wind across a rarefaction (e.g., C1 to D1) (for CIR details, see, e.g., Owens & Forsyth, 2013, and references therein). As the shock passes Jupiter and the density decreases, Jupiter's magnetosphere will expand. These CIRs recur with solar rotation (e.g., D2-E2-F2 is one solar rotation after D1-E1-F1), and their consequent compressions and expansions of Jupiter's magnetosphere are also expected to recur. For further inspection of the solar wind evolution measured by New Horizons SWAP instrument in this interval, see the supporting information.

SWAP provided solar wind velocity measurements upstream of Jupiter for only three of the X-ray observations before passing into Jupiter's magnetosphere. We attempted to leverage the SWAP measurements to further interpret the subsequent three observations by (a) searching for signatures that repeated with solar rotation to predict the recurrence of compressions/expansions from, for example, corotating interaction regions and (b) using SWAP to validate propagated solar wind conditions from 1 AU using the mSWiM

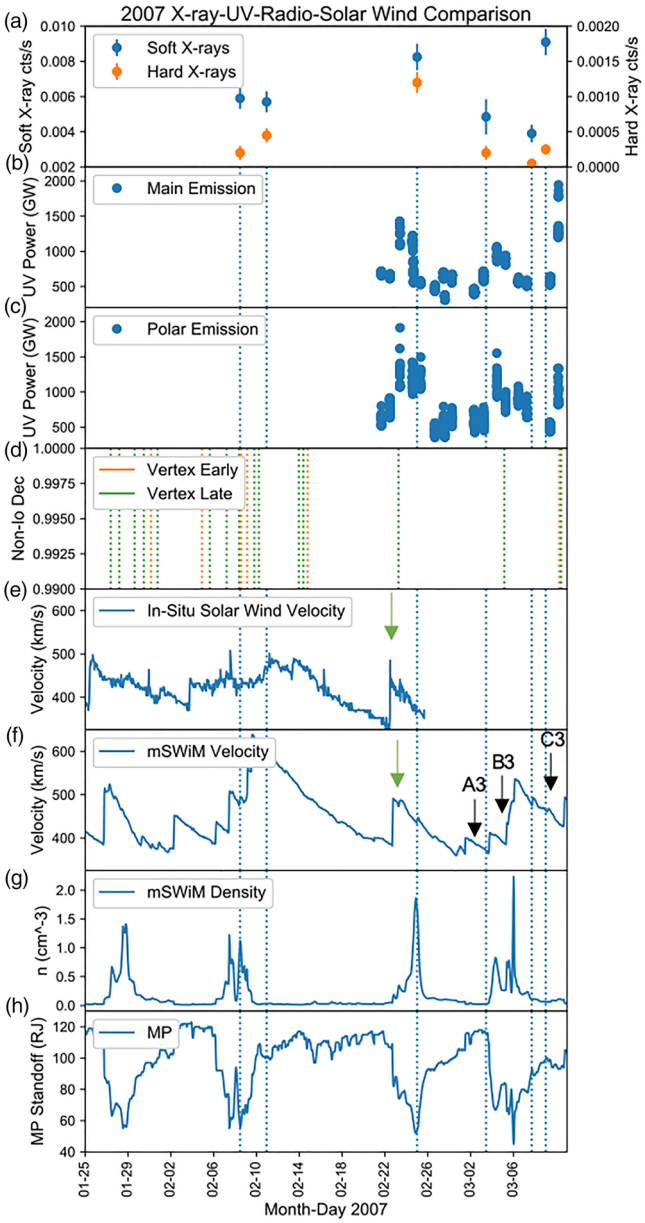

Figure 2. Multiwaveband comparisons with solar wind conditions. (a) Chandra ACIS northern aurora soft and hard X-ray counts per second for each observation (tracked through subsequent panels by blue dotted lines). Total power for the (b) UV main aurora and (c) polar aurora from HST. (d) Times of non-Io vertex early (orange) and late (green) emissions (Table 2). (e) New Horizons SWAP solar wind peak velocity upstream of Jupiter. mSWiM propagations from 1 AU of solar wind velocity (f), density (g), and mSWiM dynamic pressure driven Joy et al. (2002) model magnetopause stand-off distances (h). f, g, and h have been shifted so that the velocity discontinuity E2 in the SWAP and mSWiM velocities is aligned (vertical green arrow) and so that the arrival of shock ABC occurs a solar rotation later than observed by New Horizons at A3B3C3, which coincides with the UV auroral morphology change. As shown by Nichols et al. (2009b) and through auroral comparisons with New Horizons in situ data, the shift in the mSWiM data is not constant but varies for CIR ABC versus CIR DEF. We interpret the X-ray data assuming different shifts for each CIR. Unshifted data are shown in the supporting information.

(Zieger & Hansen, 2008) and Tao models (Tao et al., 2005), which provided insight into the solar wind density which could not be derived from the SWAP data. For example, New Horizons passed into Jupiter's magnetosphere before being able to measure the third recurrence of CIR A-B-C (A3-B3-C3). Assuming recurrence with solar rotation, the shock B3 should recur on DOY 62-63 (3–4 March) (see Figures 1 and 2).

During this campaign, Jupiter was 3–4 months from opposition (5 June 2007), so propagation models were particularly unreliable (uncertainties ~2 days), we therefore utilized them cautiously. The propagation models do show the same recurring CIRs and associated shocks as the New Horizons data, but there are differing time shifts between the models and in situ arrival of the two shocks (also found by Nichols et al., 2009b). To utilize the density propagations, we shift the propagation by +1 days, to align the SWAP peak in solar wind velocity at E2 with the same mSWiM velocity peak (green arrow on Figures 2e and 2f), then −1 days to bring the CIR A3-B3-C3 in line with its expected arrival from the SWAP data (Figure 2f) and UV auroral morphology change. For consistency with Nichols et al. (2009b), we show mSWiM in the main text (Figure 2), but there is good agreement between the Tao model, and the complete unshifted propagations from 1 AU are shown in the supporting information.

Combining the density propagations with the solar wind velocity provides insight into the dynamic pressure experienced by Jupiter. In combination with the Joy et al. (2002) model, this estimates the magnetopause standoff distance as shown in Figure 2h.

4. UV Observation Analysis

The 2007 UV aurorae are analyzed in detail in Nichols et al. (2009b), Clarke et al. (2009), and Stallard et al. (2016). Figures 2b and 2c reproduce the UV auroral powers shown in Nichols et al. (2009b), updating these for kR/power conversion factors for an absorbed to unabsorbed color ratio of 2.5 as discussed in Gustin et al. (2012). Comparing these powers with the X-ray emissions in Figure 2a shows that the northern auroral hard X-ray emission appears to only be significant for UV main emission powers greater than 1 TW. For the other X-ray observations, the hard X-ray emission is below 0.0005 counts/second, and the contemporaneous UV main emission is less than 700 GW.

Comparing the power variations with the incidence of solar wind compressions (Figure 2h) shows the correlation between UV auroral power and compressions of the magnetosphere. In Figure 3, we show that the UV aurora also clearly exhibits very similar morphological responses in phase with the evolution of both CIR D2-E2-F2 and A3-B3-C3.

Prior to the CIR (21–22 February and 2–3 March), the main oval is thin and occurs along the dashed average location contour defined by Nichols et al. (2009b) . There are intermittent “swirls” of emission in the high latitude swirl region and bright flashes/flares from what Pallier and Prangé (2001) describe as the cusp spot. When the CIRs arrive (23 February and 4 March), the main oval significantly thickens and moves poleward on the dawnside. From noon to dusk, the main emission is found at higher latitudes. This polar dusk arc emits bright pulses 20–30 min apart. On 4 March, “the cusp spot” is still observed through bright flashes. One day after the shock arrival (24 February and 5 March), the thick polar dusk arc splits into multiple arcs, which exhibit pulsations at their equatorial edge and bifurcate into extensions across the polar region. Two days after the shock arrival (25 February and 6 March), bright flares continue to be produced. For 6 March, there are no longer discrete arcs, only a single thick and pulsing arc. Upwards of 3 days after the CIR, the solar wind returns to rarefied conditions (26–27 February and 7–9 March), and Jupiter's magnetosphere would be expected to expand. The main oval responds to this by dimming and returning to lower latitudes, while the polar emissions shifts to sporadic pulses across a broader polar region.

Using the classification of auroral morphologies defined by Grodent et al. (2018), the images evolve from “Narrow”/“Unsettled” at the beginning of each interval, through to “Injections/eXternal perturbation” during the CIR compressions and returning to “Narrow/Unsettled” in the recovery and rarefaction intervals.

5. Radio Observation Analysis

Hess et al. (2012, 2014) showed that non-Io bursts of decametric emission (DAM) are triggered by solar wind compressions or rarefactions. Expansions of the magnetosphere trigger DAM with both vertex early (similar to an opening parenthesis) and vertex late (a closing parenthesis) morphology, while compressions only trigger vertex late DAM emission. The shape of these arcs results from the combination of the motion

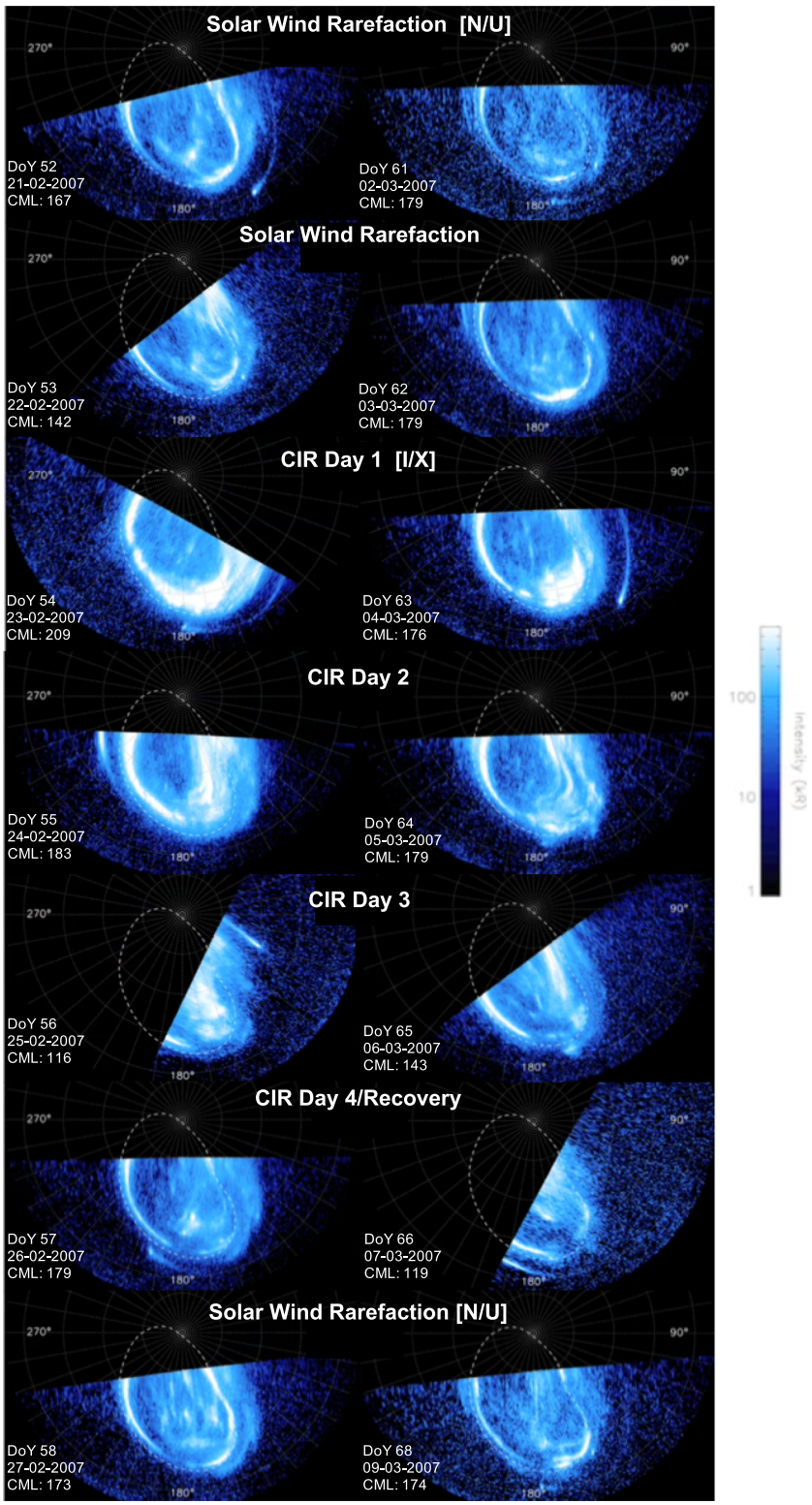

Figure 3. UV auroral images as close to CML 180° as possible. These show the auroral morphology in phase from solar wind rarefaction through the two CIR-induced shocks (D2-E2-F2 from Figure 1 in the left column and A3-B3-C3 from Figure 2 in the right column) and back to rarefied solar wind. In square brackets are the Grodent et al. (2018) categories of UV auroral morphology indicating the start times of Narrow/Unsettled (N/U) morphology and Injection/eXternal perturbation morphology (I/X) and the subsequent evolution through these states. Each image is a ~2 min exposure. Images are reproduced from supporting information from Nichols et al. (2009b).

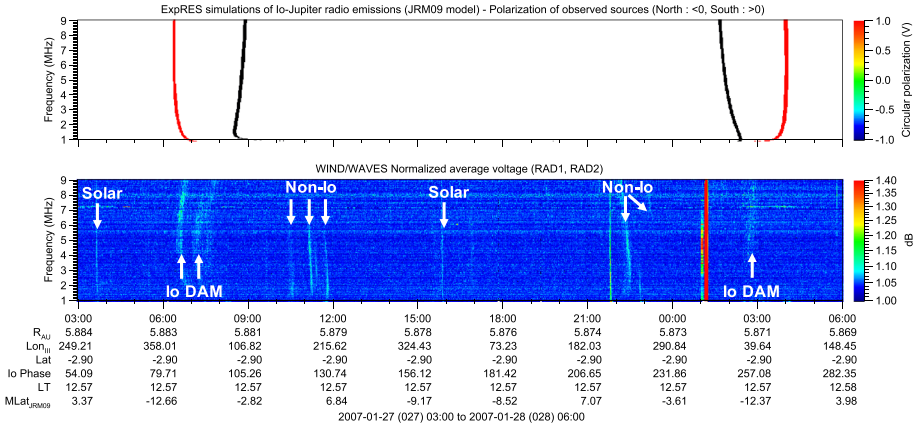

Figure 4. (a) ExPRES radio spectrogram simulations of northern (black) and southern (red) Io-DAM arcs (for details, see Louis et al., 2017, 2019) observed on 27–28 January 2007 and (b) radio spectrograms recorded by the WAVES instrument on the Wind spacecraft (total flux density). ExPRES simulates the times and morphology of the radio emissions from Io, which through comparison with the Wind/Waves data permits identification of the Io and non-Io emission labeled. Arrows indicate Io decametric emission and non-Io decametric emissions and also solar emissions.

of the source with respect to the observer and the hollow conical shape of the structure (see, e.g., Hess et al., 2014, for more details).

Using the catalogue produced by Marques et al. (2017) and by surveying the Wind/Waves (1–15 MHz) measurements, we collated the non-Io decametric emissions from January to March 2007 (Table 2). We filtered out the DAM arcs produced by the Io-Jupiter interaction through ExPRES simulations (detailed in Hess et al., 2008; Louis et al., 2017, 2019). The Wind/Waves spectrograms and ExPRES simulations for Table 2 can be found in the supporting information. We disregarded the WIND/Waves data between 9.5 and 15 MHz due to extensive radio frequency interference bands.

Figure 4 shows an example of an interval that shows both types of emission on 27 January 2007. Figure 4b shows that between 07:00–08:00 (DOY 27 2007) and 02:00–03:00 (DOY 28 2007), the decametric arcs observed at less than 9 MHz by Wind/Waves are a good fit to the simulated vertex early and vertex late Io arcs shown in Figure 4a. Figure 4b also shows decametric arcs between 10:00 and 12:00 that cannot be attributed to Io (Figure 4a) and are of the vertex late morphology associated with solar wind compressions (Hess et al., 2012, 2014). Indeed, the in situ solar wind data show that solar wind compression E1 occurred within 1 Jupiter rotation of this burst, suggesting a connection between the two. Additional bursts of decametric emission occur ~12 hr after these bursts between 22:00 and 23:30; this may be the same radio source on active field lines seen at 10:00 subcorotating back into view.

Figure 2 shows the timing of these radio emissions relative to the X-ray and UV emissions and solar wind conditions. This shows that all the non-Io decametric arcs detected during the HST campaign were contemporaneous with UV main and polar auroral brightening. Most detected arcs appear to occur within 2 days of forward or reverse solar wind shocks, with the possible exceptions of the arcs on 13–14 February and 10 March, for which there were no clear solar wind shocks.

The vertex early and late decametric arc morphology observed on 10 March occurred within the same Jupiter rotation as the brightest UV main emission of the campaign (power ~ 2–4 TW) and during an increase in brightness of the polar emissions by a factor of 4 (up to ~2 TW). The observation on 10 March was abnormally bright and exhibited auroral morphology which may fit one of three different criteria outlined by Grodent et al. (2018). The dawn storm feature has a morphology most like an injection event auroral morphology. These typically develop over time scales of a Jupiter rotation and can be internally driven. Given that solar wind propagations were not suitable at this time due to the large Earth-Sun-Jupiter angle, we also explored the SOHO-LASCO ICME catalogues to test whether a radially moving ICME may not have appeared in the solar wind propagations. Unfortunately, we were unable to draw a firm conclusion as to whether this significant brightening of the UV aurora and these early and late vertex non-Io arcs were internally or externally driven. For further details, see the supporting information.

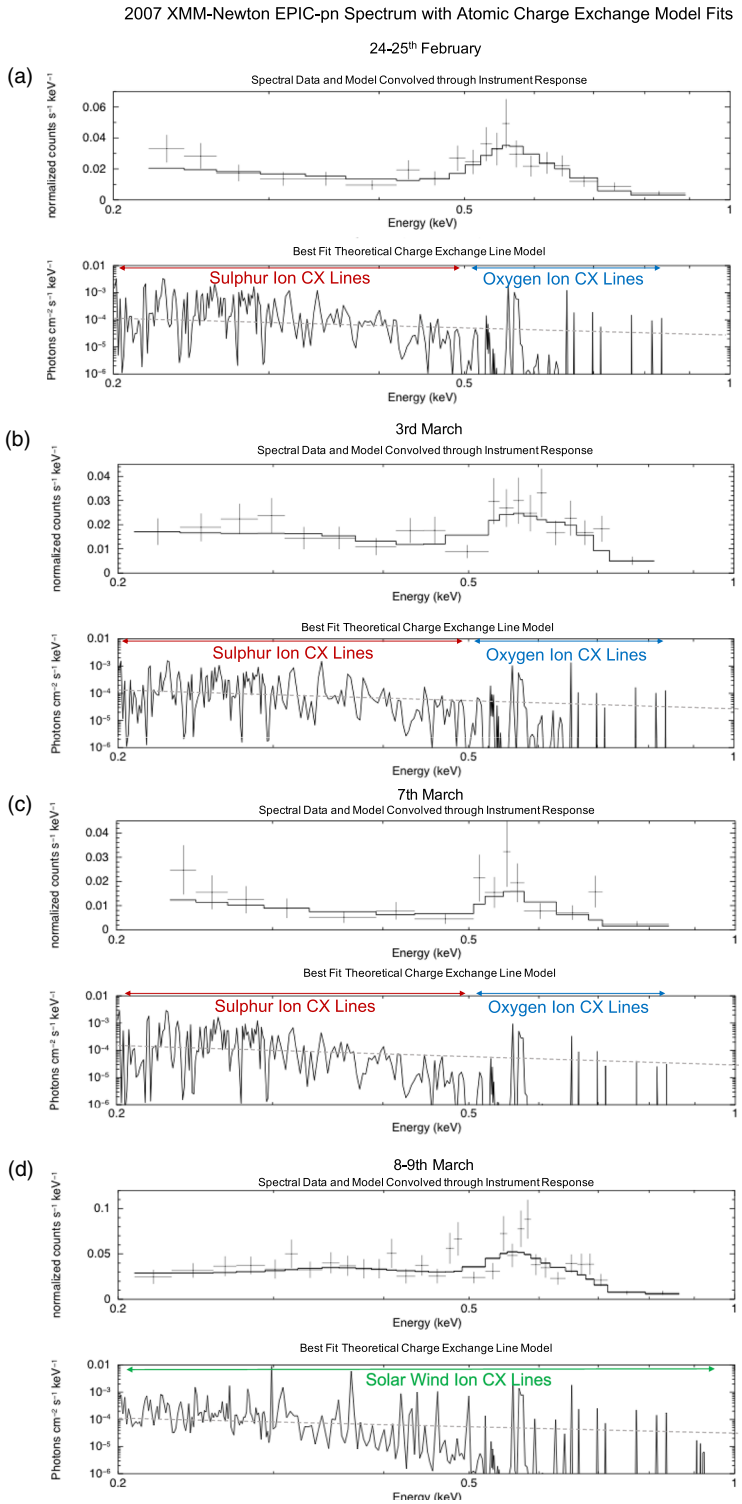

Figure 5. XMM-Newton EPIC-pn Northern Aurora spectral data from 2007 with their respective best-fit charge exchange models for (a) 24–25 February, (b) 3 March, (c) 7 March, and (d) 8–9 March. Upper panels, respectively, are the best-fit atomic charge exchange spectral models convolved through the instrument response (black line) and plotted with the XMM-Newton EPIC-pn observation (crosses). Lower panels, respectively, show the best-fit theoretical atomic charge exchange models of iogenic ions (sulfur + oxygen) or a solar wind ion population (composition based on in situ measurements in Von Steiger et al, 2000), with bremsstrahlung continuum where this provided an improved fit. The dashed line on charge exchange models illustrates the cutoff for spectral lines expected to produce a signature at greater than 0.01 normalized counts per s per keV.

Table 3
Best-Fit Parameters for Iogenic (S+O) and Solar Wind (SW) Atomic Charge Exchange (CX) Model Fits to the XMM-Newton EPIC-pn Northern Auroral Spectra

Date	χ^2 of fit	kT (keV)	CX Flux (ph/cm^2/s)	S:O	Bremsstrahlung
24–25 Feb S + O	0.85	0.19 ± 0.01	$2.0 \pm 0.1 \times 10^{-6}$	0.8	Yes
3 March S + O	1.1	0.26 ± 0.05 7 ± 3 x 10^{-7}	0.9	No	
7 March S + O	0.89	0.11 ± 0.04	$7 \pm 3 \times 10^{-6}$	0.6	No
8–9 March S + O	1.3	0.25 ± 0.04	$1 \pm 1 \times 10^{-6}$	1.24	No
24–25 Feb SW	1.16	0.22 ± 0.01	$2.0 \pm 0.2 \times 10^{-7}$	N/A	Yes
3 March SW	1.1	0.23 ± 0.02	$1.7 \pm 0.2 \times 10^{-7}$	N/A	No
7 March SW	1.2	0.19 ± 0.02	$1.1 \pm 0.3 \times 10^{-7}$	N/A	No
8–9th March SW	1.0	0.19 ± 0.01	$4.6 \pm 0.5 \times 10^{-7}$	N/A	No

Note. This shows for each observation: the χ^2 of the best fit model, the temperature of the ion distribution, the photon fluxes produced from ion charge exchange, the ratio of S:O, and whether a Bremsstrahlung continuum improved the fit. We note that the temperature of the distribution is not built to reflect the complexity of the collision of ions with Jupiter's atmosphere but provides a useful qualitative diagnostic of the energization of the population during different intervals (see Dunn et al., 2020, for details).

6. X-ray Observation Analysis

6.1. Interpreting the Conditions During Each X-Ray Observation

The observation on 8 February occurs during the second compression of the magnetosphere within a few days, while 10–11 February occurs when the magnetosphere has expanded back to ~100 R_J. The 24–25 February is the peak of solar wind compression D2-E2-F2 with a magnetopause standoff distance of ~50 R_J. It may be that the 8 February observation is dimmer than 24–25 February because, as found by Kita et al. (2016), the magnetosphere had already been in a compressed state very recently; 3 March is either at the end of a prolonged period of stable rarefied slow solar wind or at the start of a solar wind compression from CIR A3-B3-C3. Conditions on 7 and 8–9 March seem to occur when the magnetosphere is expanding back to ~100 R_J following a prolonged interval of compression.

6.2. X-ray Spectra

In the companion paper to this (Dunn et al., 2020), we introduce the method for fitting Jupiter's X-ray auroral spectra with atomic charge exchange spectral line lists from AtomDB (http://www.atomdb.org/ - Smith et al., 2012) and contrast fits for Chandra ACIS with XMM-Newton EPIC spectra. That analysis showed that Chandra ACIS appears to systematically under-report Jovian auroral emission between 0.45 and 0.6 keV, which is key for studies of the oxygen emission in the spectrum. Here, we therefore focus on the XMM-Newton EPIC-pn spectra and follow the spectral extraction and fitting methods outlined in the companion paper.

Figure 5 shows the best-fit models and spectra for each observation, while Table 3 shows their best-fit parameters. The 24–25 February was the only observation where adding a bremsstrahlung continuum provided a better fit. This supports the low hard X-ray counts recorded by Chandra (Figure 2a) and suggests that bright hard X-ray emission may not be common and may be triggered by solar wind compressions.

For each observation, we compared charge exchange spectrum models for a precipitating iogenic ion population (sulfur + oxygen), suggesting a magnetospheric source for the precipitating ions, with a solar wind ion population (using the ion abundances in Von Steiger et al., 2000). We found that for 24–25 February and 7 March, an iogenic ion population provided a better fit to the data (Table 3). Figure 5 shows that the 8–9 March spectrum is clearly morphologically quite different from the 24–25 February and 7 March spectra. The rising rather than falling emission from 0.2 to 0.35 keV and emissions between 0.4 and 0.5 keV were better fitted by a solar wind ion population, than a purely sulfur and oxygen population, suggesting that solar wind ions precipitated in Jupiter's polar region at this time. The 3 March spectrum shares morphological features with both an iogenic population and solar wind population and both models were able to produce an equally good fit to the spectrum.

6.3. Auroral Morphology

The spatial, spectral, and temporal resolution of Chandra ACIS allowed us to reregister the X-rays photons to their Jovian System III (S3) latitude-longitude positions so that the different spatial distributions of the

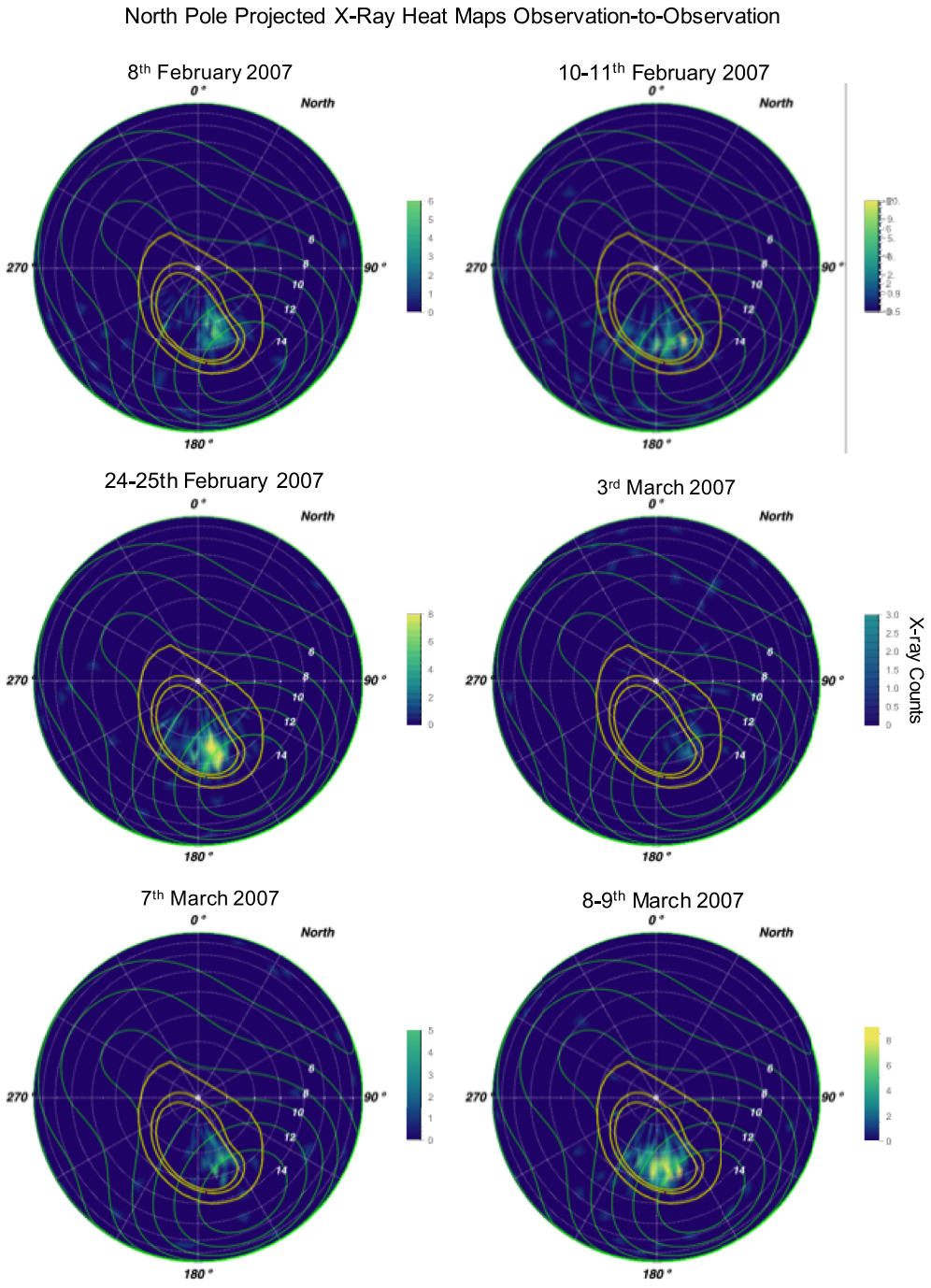

Figure 6. Chandra ACIS projected X-ray density maps centered on Jupiter's north pole, showing the 0.2–5 keV energy range of emission. The logarithmic color bar indicates the number of X-rays in bins of 3° by 3° of S3 latitude-longitude. All projections are scaled to saturate the color bar at 8 counts. Dashed gray lines of longitude radiate from the pole, increasing clockwise in increments of 30° from 0° at the top. Concentric gray circles outward from the pole represent lines of latitude in increments of 10°. Thin green contours with white text labels indicate the VIP4 (Connerney et al., 1998) model magnetic field strength in Gauss. Thick gold contours show the magnetic field ionospheric footprints of field lines intersecting the Jovigraphic equator at 5.9 R_J (Io's orbit), 15 R_J, and 45 R_J (Grodent et al., 2008; Vogt et al., 2015) from equator to pole, respectively.

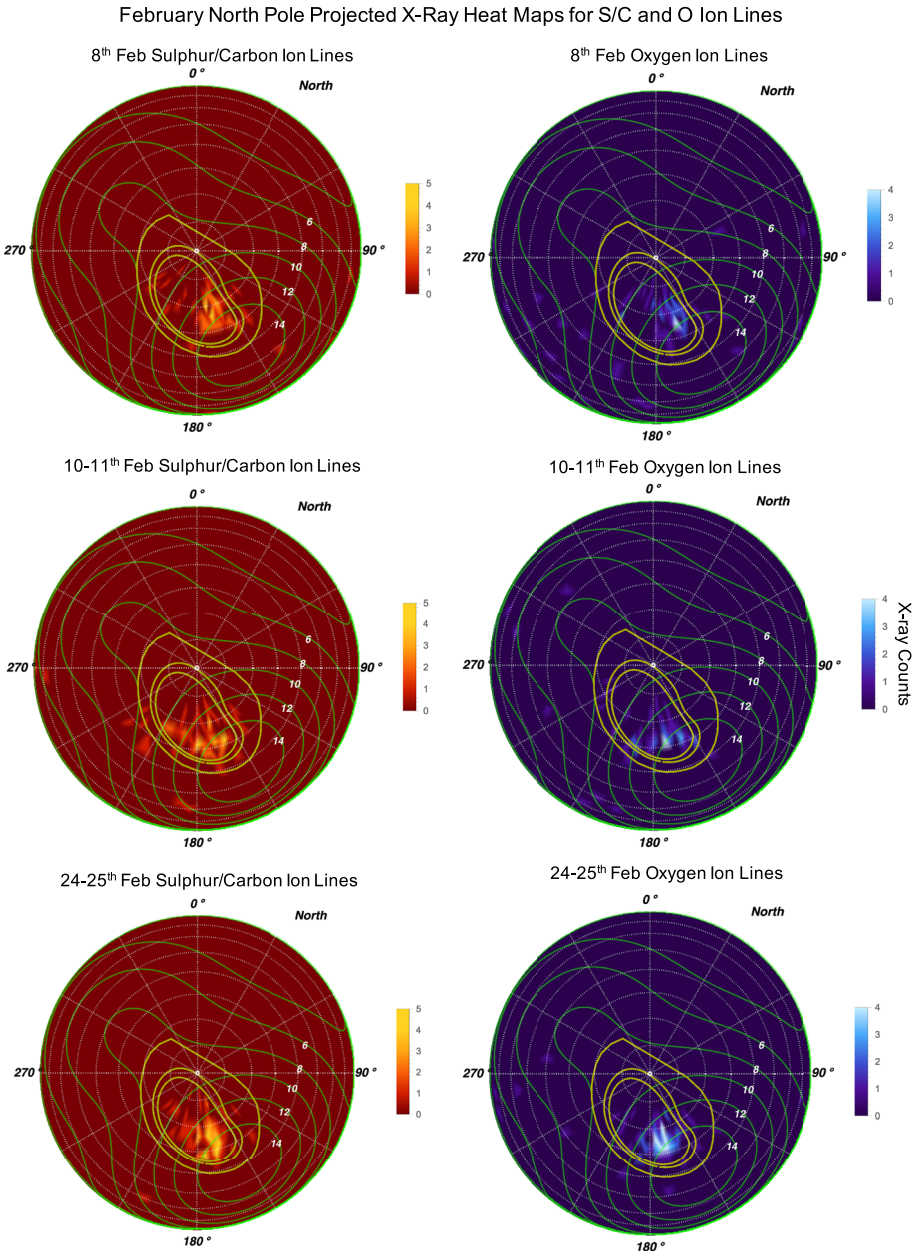

Figure 7. Projected density maps centered on Jupiter's north pole from Chandra ACIS, comparing the 200–500 eV emission from sulfur/carbon ions (left) with the 500–900 eV emission from oxygen ions (right) for the February 2007 observations, with both scaled to saturate the color bar at 5 counts. For further details, see Figure 6.

aurora could be explored. At latitudes equatorward of the auroral zone, there are sparsely distributed X-ray emissions from solar X-ray photons scattered in Jupiter's atmosphere. Figure 6 shows that while the X-ray aurora is always dominantly poleward of the UV main emission (as defined by contours mapping to 15 and 45 R_J; Vogt et al., 2015) , the X-ray aurora morphology does vary. For the observations when the magnetosphere is compressed (e.g., 8 and 24–25 February), the X-ray aurora is concentrated into a localized bright region within longitudes up to 180°, while for the expanded magnetosphere cases, it is more patchy and extended across the polar region (e.g., 10–11 February and 8–9 March). The 8 and 10–11 February observations have almost identical CML coverage showing that this changing spatial extent is not due to different visibility. These differences may suggest a link between the X-ray morphology and the magnetosphere size or solar wind conditions.

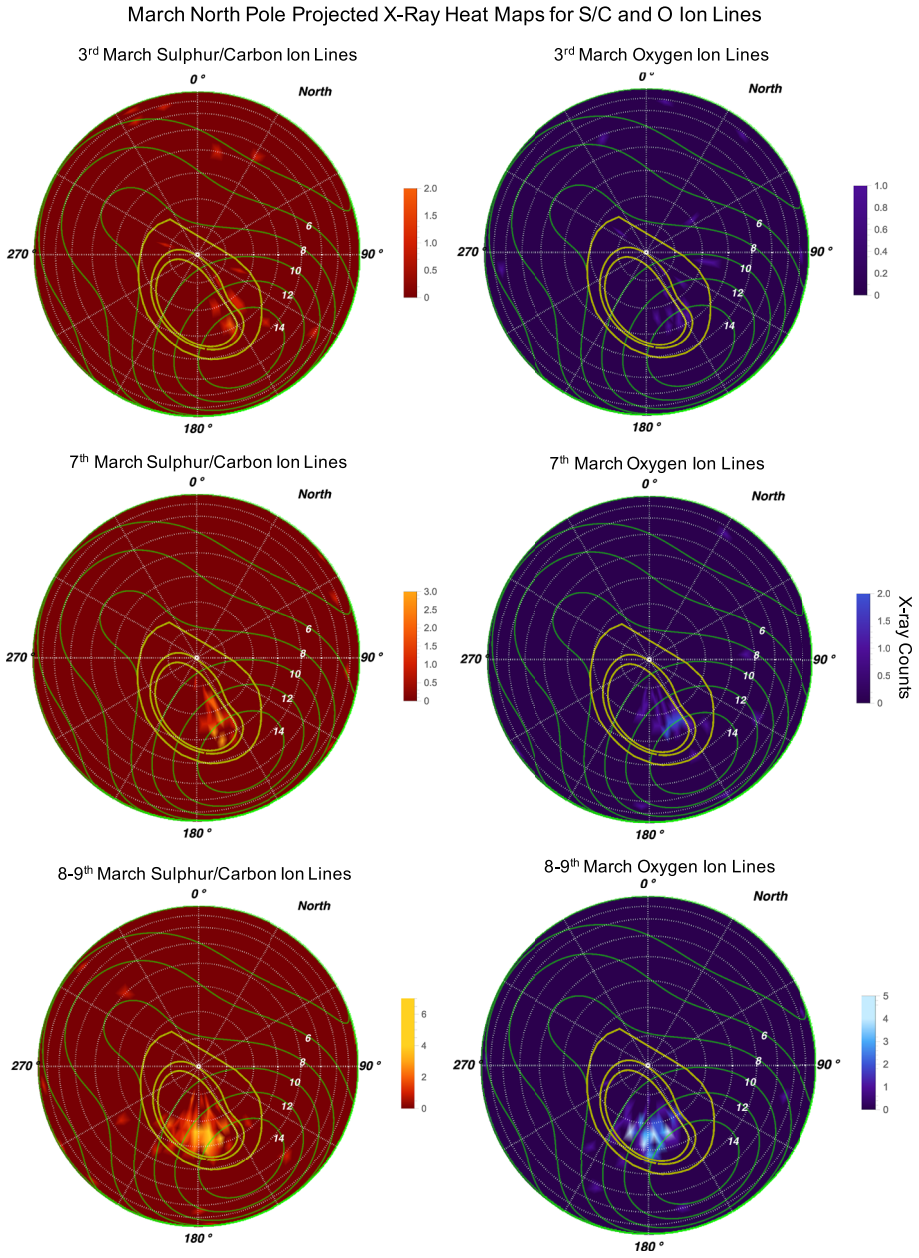

Figure 8. Projected density maps centered on Jupiter's north pole from Chandra ACIS, comparing the 200–500 eV emission from sulfur/carbon ions (left) with the 500–900 eV emission from oxygen ions (right) for the March 2007 observations, with both scaled to saturate the color bar at 5 counts. For further details, see Figure 6.

Polar projections for the ion energy bands of 0.2–0.5 keV (sulfur/carbon emission) and 0.5–0.9 keV (oxygen emission) (Figures 7 and 8) suggest that oxygen emission is typically more localized, while sulfur emission is more broadly distributed. As discussed by Dunn et al. (2016), sulfur requires less energy to generate X-rays so this may demonstrate differing distributions of potential drops across the pole.

Figure 9 contrasts the X-ray electron bremsstrahlung spatial distribution with the distribution from ion lines (0.2–0.5 keV). There are only two observations with a significant hard X-ray signal. For 10–11 February, the emission is very dim and along the expected location of the UV main emission. For 24–25 February, in the dawn sector, the hard X-rays are along the expected main emission location, but in the dusk sector, they are shifted poleward of this. The UV main emission was particularly bright (power of ~1 TW; see Figure 2) during this interval and was also shifted polewards in the dusk sector (Figure 3) such that the hard X-rays are still colocated with the UV main emission location. For the other X-ray observations, the UV main emission

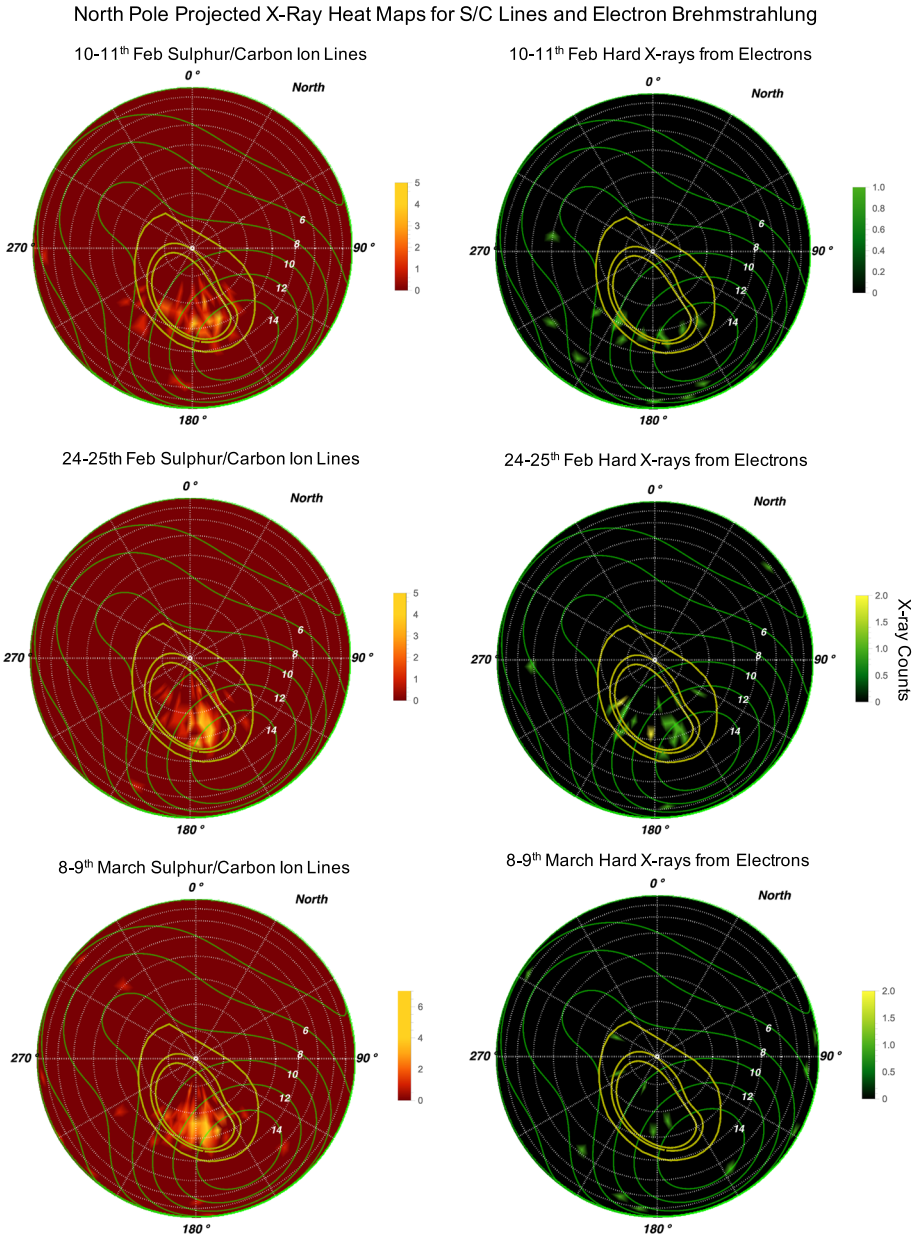

Figure 9. Projected density maps centered on Jupiter's north pole from Chandra ACIS, comparing the 200–500 eV emission from sulfur/carbon ions (left) with the greater than 1 keV emission from electrons for observations on the 8 February (top), 24–25 February (middle), and 8–9 March (bottom) 2007. For further details, see Figure 6.

power was around 500 GW, and the hard X-ray emission appears to be very low (~1 count per hour for Chandra ACIS).

The 24–25 February hard X-rays also seem colocated with soft X-rays from precipitating ions. It could be that this region produces high energy electron and ion precipitation or that they are so closely located that Chandra's spatial resolution would not resolve their separation. Figure 9 also hints at some possible emission on 10–11 February close to Io's footprint at around 240° S3 longitude. Here, the surface magnetic field strength decreases which would allow drifting and/or bouncing particles to more easily access the atmosphere, since the mirror point would be closer to the atmosphere. However, we note that these photons were emitted close to the observed limb of the planet, and therefore, the obliquity of the viewing angle may mean that the emission is projected closer to the Io footprint than its true origin location. Establishing whether these photons are indeed from the Io flux tube or Io Plasma Torus will therefore require additional exploration with observations with a more favorable viewing geometry.

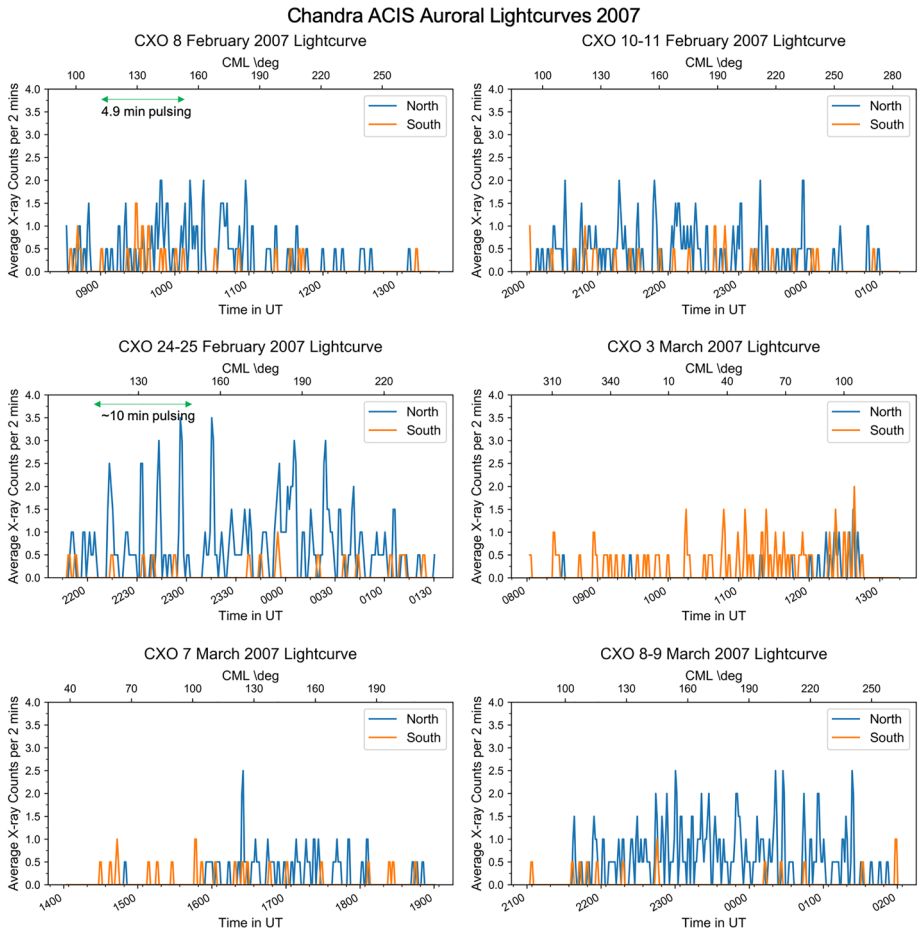

Figure 10. Chandra ACIS X-ray lightcurves from the northern (blue) and southern (gold) aurora for each observation. Central meridian longitude is indicated across the top, while time is along the bottom of the *x*-axis. The lightcurves are 1-min binned, with 2-min moving-average smoothing. The green horizontal arrows show intervals when power spectral density plots (Figure 13) show hints of regular pulsations.

6.4. Timing Signatures

We present Chandra and XMM-Newton auroral lightcurves but expect differences because of each instrument's energy-dependent responses and because Chandra's higher spatial resolution permitted lightcurve extraction from S3 coordinates centered on the aurora (extracted above 55° latitude), while XMM-Newton's lower spatial resolution meant all emissions from the northern or southern polar region were used.

The northern aurora lightcurves reveal changing behavior from observation to observation (Figures 10 and 11). By examining how X-ray counts are distributed across time bins and through fast Fourier transforms (FFTs) of the lightcurves, we identify three types of temporal behavior exhibited by Jupiter's X-ray aurora during 2007: regular pulsed behavior, irregular pulsed behavior, and “flickering” emission. The pulsed behaviors occur when the X-rays are concentrated into short-lived, (1–2 min duration) impulsive bursts of emission which are bounded by long intervals of dim no emission between each burst. Examining the distribution of counts across time bins and the change in counts from each time bin to the next shows two statistical characteristics of pulsed behavior: The distribution of the change in counts per time bin is highly peaked (Figure 12), and consequently, the coefficient of variation (the standard deviation divided by the mean) is larger for pulsed intervals (Table 4), for each respective instrument.

Power spectral density (PSD) analysis, such as that produced by FFTs, confirms whether pulses occur regularly or not (Figure 13). The 8, 10–11, and 24–25 February and 7 March all exhibited pulsed behavior. The 8 February has regular intervals of ~5 min between each pulse from 09:00 to 10:30 UT, and 24–25 February appears to have ~10 min periodicity from 22:00 to 23:00, although this is less statistically significant in the FFTs. Jackman et al. (2018) also reported a regular 4.9 min pulsation period with a 96% confidence for the

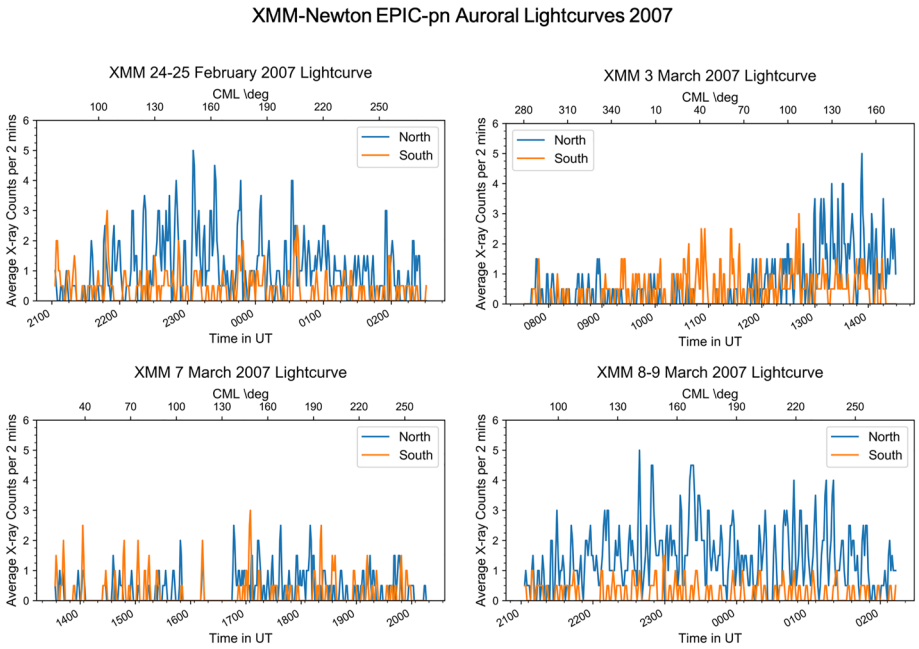

Figure 11. XMM-Newton EPIC-pn X-ray lightcurves from the northern (blue) and southern (gold) aurora for each observation. Central meridian longitude is indicated across the top, while time is along the bottom of the *x*-axis. The lightcurves are 1-min binned, with 2-min moving-average smoothing.

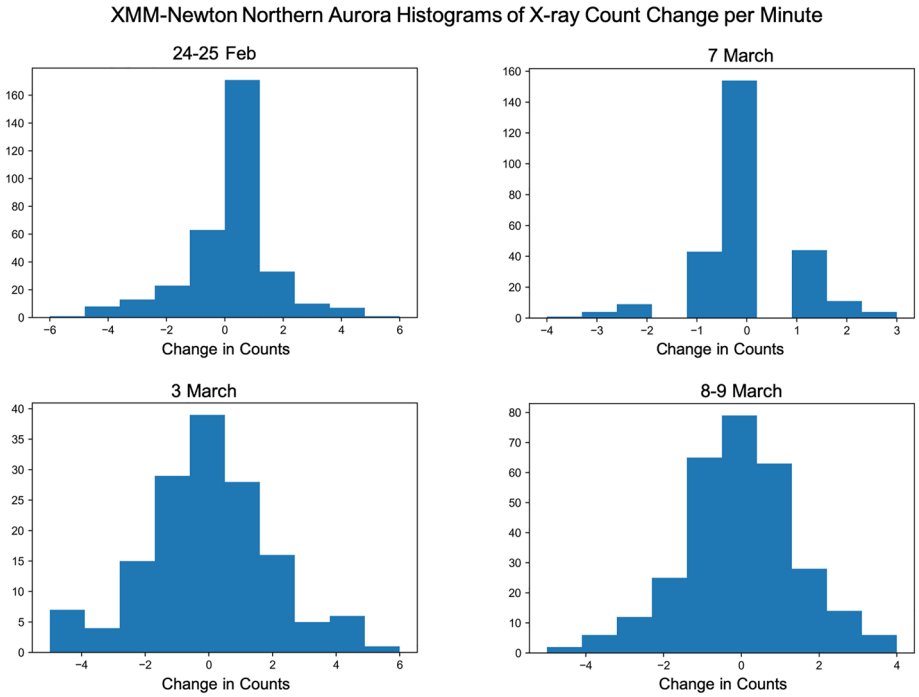

Figure 12. Histograms of the XMM-Newton northern aurora showing how the number of counts in each 1-min time bin changes from one time bin to the next. These show two possible behaviors in the timing of emission: highly pulsed emission (24–25 February and 7 March) versus short time interval (1–2 minute) small changes in emission that we define as "flickering" X-ray aurora (3 March and 8–9 March).

Table 4
Means (μ), Standard Deviations (σ), and Coefficients of Variation ($\frac{\sigma}{\mu}$) for the Number of Counts Per 1 min Bin for the Northern Aurora During 2007

Observation	μ	σ	$\frac{\sigma}{\mu}$	Temporal behavior
CXO 8 Feb	0.3	0.7	2.33	Regular pulses
CXO 10–11 Feb	0.4	0.7	1.75	Ir/regular pulses
CXO 24–25 Feb	0.6	1.0	1.67	Regular pulses
CXO 7 Mar	0.2	0.5	2.5	Irregular pulses
CXO 8–9 Mar	0.6	0.8	1.33	Flickering + irregular pulses
XMM 24–25 Feb	1.0	1.3	1.3	Regular pulses
XMM 3 Mar	1.3	1.4	1.08	Flickering + irregular pulses
XMM 7 Mar	0.4	0.7	1.75	Irregular pulses
XMM 8–9 Mar	1.4	1.3	0.93	Flickering + irregular pulses

Note. The final column summarizes the temporal behavior of the X-ray aurorae during each observation as determined from the combination of lightcurves, histograms, and fast Fourier transforms (Figures 10, 11, 12, and 13).

8 February observation, but this included the entire time window and was not filtered by system III coordinates, as the PSDs shown here are. For the pulsed behavior on 10–11 February and 7 March, the PSDs do not show any strong regularity.

What we define as "flickering" behavior can also appear to be steady emission if the time bins of the aurora are larger than 1 min or if it is smoothed as shown in Figures 10 and 11. This behavior is a short time scale (1–2 min) variable dim (not as bright as pulses) emission of photons, which is continuous for several hours (i.e., does not have prolonged intervals without emission). Flickering behavior is characterized by a broader structure for the distribution of changing counts per bin (Figure 12) and smaller coefficients of variation (Table 4), for each respective instrument. Inspection of the northern aurora XMM lightcurves for 3 and 8–9 March shows these "flickering" or steady emissions superposed with pulsed emissions. For example, 8–9 March has comparably bright flares to 24–25 February, but the interval between these bright flares is populated by this flickering or steady emission. There are also intervals of heightened continuous X-ray emission, such as that between 23:15 and 23:30 on 8–9 March, when XMM continuously detects three to five X-rays every minute from the aurora. This 15 min interval produces almost as much auroral X-ray emission as the entire 7 March observation. A similar prolonged bright enhancement was also observed in 2011 (Dunn et al., 2016). While the short duration (approx. 1 min) pulses are sometimes colocated with UV flares (Elsner et al., 2005), neither the X-ray "flickering" nor the structure that lasts ~15 min has yet been connected to UV emissions.

7. Summary of Results and Discussion

The combination of the solar wind measurements and radio emissions suggest that corotating interaction regions compressed Jupiter's magnetosphere between 4–5 and 22–23 February and 3–4 March 2007. The magnetosphere then expanded back to an uncompressed state between 9–10 and 26 February and 7–10 March, respectively. The UV aurora clearly evolves in phase with these compressions, as catalogued here and in Nichols et al. (2009b) and Grodent et al. (2018). The majority of the detected non-Io decametric emissions also appear to be well aligned with solar wind shocks and occur contemporaneously with UV polar and main emission auroral brightening. Any connection between the non-Io decametric emissions and X-ray aurorae is less evident.

7.1. X-Ray Trends with Solar Wind Conditions

These observations presented a rare opportunity to compare Jovian auroral emissions with a measurement of solar wind conditions just upstream of Jupiter. In contrast with previous work using propagation models, we did not find a correlation between solar wind velocity and X-ray emissions. The emissions were brightest during the lowest solar wind velocity and dimmest during faster solar wind, although the velocity difference was small (~50 km/s; Figure 2). Clearly though, as with the UV aurora, Jupiter's X-ray aurora can be modulated by solar wind shocks; the observation on 24–25 February is affected by a solar wind shock,

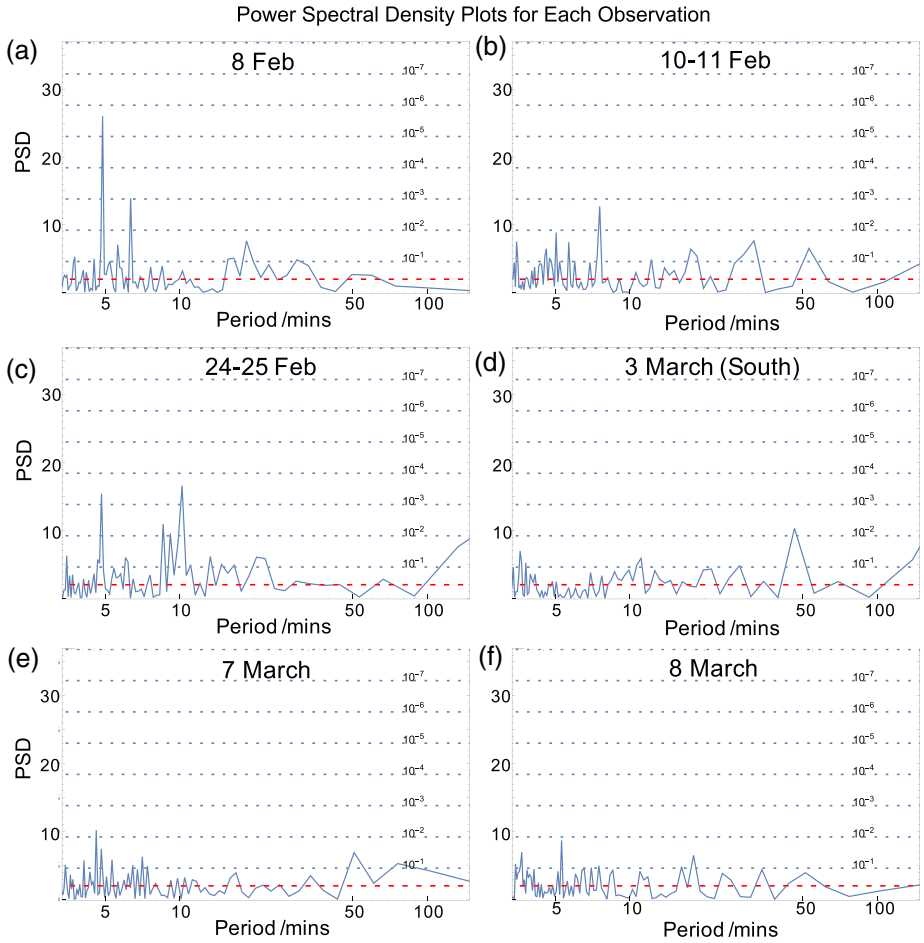

Figure 13. Power spectral density (PSD) plots from fast Fourier transforms of the Chandra X-ray lightcurves from the X-ray hot spots in 2007, following the normalization and significance methods laid out in Leahy et al. (1983) and first applied to Jupiter in Elsner et al. (2005). The dashed red lines show the value obtained for Poisson statistics applied to a steady source (i.e., if the source signal was not pulsed but still had low counts subject to Poisson statistics). The dotted horizontal lines show single-frequency probability chance occurrences (PCO) for the detected periods. The lowest statistical significant and highest PCO of 10^{-1} is at the bottom of the plot. Lightcurves were extracted from 155° to 180° longitude and poleward of 60° latitude for the northern hot spot and 30° to 80° longitude and poleward of −65° latitude for the southern hot spot.

and Dunn et al. (2016) also show evidence for shock-driven enhancements. However, the brightest observation of the 2007 campaign (8–9 March) occurs during modest solar wind velocities and low densities, and when the UV aurora does not exhibit compression morphology, suggesting an expanding/expanded magnetosphere. The very bright 8–9 March observation may suggest that either (a) the interplanetary magnetic field direction is critical to producing these additional signatures (it was unmeasured for this campaign) or (b) that internal magnetospheric variations and/or processes during expansion are also able to modulate the X-ray aurora behavior. Here, we attempt to collect and categorize the behaviors observed.

7.2. Forward Shock Driven X-Ray Aurora

The solar wind forward shock that compressed the magnetopause on 24–25 February appeared to trigger the only bright electron bremsstrahlung emission from the campaign. These emissions were coincident with shifted and expanded UV aurora main emission. Relativistic ~100 s keV electrons may be required to produce observable hard X-rays, and these may only be present with sufficient fluxes when the UV main emission has powers greater than 1 TW. These electrons would be expected to produce larger current densities and kinetic energy fluxes than their nonrelativistic counterparts (Cowley, 2006).

Given the excellent fits for a sulfur + oxygen ion population to the spectra, the X-ray pulses during compressions appear to be produced by magnetospheric plasma. This further suggests that the UV active region is

also produced by processes inside the outer magnetosphere (e.g., Bonfond et al., 2017). Under compression, these ion-produced flares occur closer to the electron bremsstrahlung emissions and to a bright pulsing dusk arc of UV emission. Mauk et al. (2017) use Juno JEDI data to show that electrons and ions can precipitate together in this region. The quasi-colocation of the electron and ion emissions may be because the outer magnetosphere processes are more spatially confined to a smaller region by the compression. Theoretical studies have also suggested that coupling currents may reverse during solar wind compression (Cowley & Bunce, 2003a, 2003b; Cowley et al., 2007; Yates et al., 2014). If the X-rays do indeed represent the downward currents, then these observations suggest that upward and downward current systems occur closer together and are possibly interspersed during compressions (e.g., Mauk & Saur, 2007 and Forsyth et al., 2014) (although X-rays only trace the most energetic ions, so this may not reflect the full extent of the downward current).

During magnetospheric compression, the X-ray aurora appears to be more localized; during expansion, the emission spreads polewards and longitudinally and is more patchy. This may delineate the halo/core structures that were identified by Kimura et al. (2016). It may be easier to generate a detectable regular periodic pulsation from a compressed magnetosphere, which would have a smaller dayside magnetosphere and therefore fewer processes occurring which could be superposed into the X-ray lightcurve. This would be consistent with the majority of regular X-ray pulsation detections being during intervals of compression (e.g., Dunn et al., 2016, 2017), including those in this paper. Alternatively, Nichols, Badman, et al. (2017) suggest that UV pulses may be the product of tail reconnection, while Guo, Yao, Wei, et al. (2018), Guo, Yao, Sergis, et al. (2018) suggest that rotation-driven reconnection may cause the X-ray aurora. Tail/rotational reconnection would be expected to be enhanced by compressions of the magnetosphere and to produce pulses of X-ray emission with spectral signatures consistent with iogenic plasma, as reported here.

7.3. Expanded Magnetosphere or IMF-Dependent X-Ray Aurora

Arguably, the most interesting but puzzling observation of the campaign is 8–9 March. It is during an interval of magnetospheric expansion that does not seem to have particularly different solar wind velocities or densities than 10–11 February or 7 March, and yet, the observation is the brightest in 2007. The spectra suggest that the precipitation of solar wind ions contribute X-ray auroral emissions at this time, while the timing signatures suggest that multiple processes produced the X-ray aurora.

The X-ray time signatures suggest a combination of bright flares superposed on flickering emission. If the X-ray emission on 8–9 March is connected to the UV aurora one Jupiter rotation later, then there are two possible counterpart UV emissions on 9 March that may explain the steady X-ray emission. The swirl region is dim but active, with low levels of emission from a few spatial locations, so that this emission may appear to "flicker." There is also a rarer long-lasting transpolar filament, which may explain the steady polar emission, coexisting with intermittent flares. Polar filaments have been suggested to relate to high latitude reconnection (Nichols et al., 2009a), and if this was the case, then they could provide a steady solar wind ion precipitation to generate the X-ray spectra observed. However, theoretical arguments show it is difficult to produce X-ray aurora through direct solar wind precipitation without bright proton auroras (Bunce et al., 2004; Cravens et al., 2003). It may therefore be easier to explain the spectral signatures if the outer magnetosphere had a mixed iogenic and solar wind population. This raises the question of how the solar wind gained entry for this interval, while it is not present in the others.

It may be that there was an interval of increased reconnection at Jupiter's magnetopause, which injected solar wind ions into the system. Alternatively, the mechanical motion of the magnetosphere during expansion may permit this solar wind entry. mSWiM propagations with the Joy et al. (2002) model suggest a magnetopause shift from ~50 to 100 R_J over the 3 days during which this observation occurs. This expansion would depend on the magnetospheric thermal plasma providing sufficient internal pressure following a compression. If the expansion of the magnetosphere occurred as a harmonic oscillator, this could help trigger formation or roll-up of Kelvin-Helmholtz instabilities (KHI), through which solar wind ions could enter the magnetosphere (Ma et al., 2017). Alternatively, during rarefied solar wind, O^{7+} ions have a gyroradius of 0.1–0.3 R_J and a gyroperiod of ~10 s of minutes (assuming velocity of 10% of the bulk and B ~ 0.2 nT, comparable to 10th percentile Bagenal et al., 2014; Ebert et al., 2014). If the magnetosphere did expand by ~50 R_J within ~3 days, the expansion rate is at a comparable time scale and length scale to the gyroperiod and gyroradii of high charge state ions in the solar wind. It may therefore be possible for solar wind ions to

simply have gyrated across the magnetopause and into the outer magnetosphere.

The broader spatial distribution for 8–9 March could reflect a variety of different possible processes, including reconnection with the solar wind. It could be indicative of a shift/redistribution of return currents across an extended magnetosphere, which may have larger potential drops due to the differing distances and densities. We also propose two other possible drivers: as at Earth, magnetospheric expansions can generate vortices in the outer magnetosphere. These vortices can produce field-aligned current systems and associated auroral emissions in locations where they might otherwise not exist (Shi et al., 2014; Zhao et al., 2016). Alternatively, an expanded/ing magnetosphere may enhance radial outward mass transport, which could enhance internal processes such as reconnection.

The limited visibility for 3 March observation combined with the uncertainties on the solar wind conditions makes it more challenging to fully categorize. However, it occurs within a few hours of an expanded magnetospheric UV aurora, and the spectrum is equally well fit by iogenic or solar wind ions (without a bremsstrahlung component). It also has temporal signatures of pulses and flickering X-ray aurora. The combination of these factors suggests a possible consistency with the 8–9 March observation or an interval of transition between expanded and compressed states.

7.4. Dim X-Ray Aurora During Shock Recovery

The 10–11 February and 7 March observations occur during magnetospheric recovery. They are all very dim due to a low rate of dim X-ray pulses. Their timing during expansions may help to distinguish between expansion and IMF-dependent auroral processes for 8–9 March. Magnetopause and magnetodisk reconnection, KHI, downward currents and wave interactions have all been proposed as mechanisms for the X-ray aurora (Bunce et al., 2004; Cravens et al., 2003; Dunn et al., 2017; Guo, Yao, Wei, et al., 2018; Manners et al., 2018). These dim observations may suggest that during shock recovery, conditions are either unfavorable for whichever process produces the X-ray emissions or that the ion densities/energies are too low.

8. Conclusion

We report trends in the responses of the X-ray, UV, and radio emissions of Jupiter during changing solar wind conditions measured by the New Horizons spacecraft in February and March 2007. A solar wind shock causes the Jovian soft and hard X-ray aurorae to brighten on 24–25 February. This is the only observation in 2007 with significant hard X-ray emission, and these hard X-rays are colocated with a UV dawn storm and dusk polar arc, with UV aurora main emission powers of ~1 TW. At this time, soft X-ray emission from ion precipitation, which may indicate the downward currents, is located more closely to the hard X-rays from the upward current system, than normally observed (e.g., Branduardi-Raymont et al., 2008), which could suggest a more interspersed upward and downward current system during magnetospheric compressions. The soft and hard X-ray emissions appear to be independent, and their relative responses can provide important clues to the state and dynamics of the magnetosphere. The rarer brightening of the hard X-ray emission acts as a tracer of solar wind compressions, while the soft X-ray ion response seems more complex and can also brighten during either magnetospheric expansions or intervals favorable to reconnection (e.g., 8–9 March).

While the polar soft X-ray emissions brighten during both forward shocks and magnetospheric expansions, their spectra are very different for the two intervals. Iogenic ion populations provide a best fit during magnetospheric compressions. For at least one bright observation with an expanding/ed magnetosphere, the emission has a spectrum that is best fit by including a population of solar wind ions. The time series data and spatial distributions of events suggest that superposed on the typical auroral pulses/flares, there is a steady or flickering X-ray source, suggesting multiple processes produce the X-ray aurora at this time. It also suggests that, while significant abundances of solar wind ions entering the system is uncommon, the conditions (IMF direction, rapid magnetopause expansion, and/or harmonic oscillations of the magnetopause) were right for this during this observation.

The 2007 campaign provides a rich multiwaveband observation campaign that demonstrates that Jupiter's X-ray aurora exhibits several different characteristic behaviors, which coincide with different solar wind and UV auroral conditions. Further observations will be required to fully constrain the correlations and driving processes for these intriguing behaviors. The analysis presented here takes important steps towards identifying these different behaviors and the possible connections with solar wind or internal drivers.

Acknowledgments
W. R. D. would like to thank D. McComas for support with the New Horizons SWAP data. W. R. D. would also like to thank the Vogt/Masters and Jackman/Paranicas ISSI team meetings, which initiated this project. W. R. D. was supported in this work by a Science and Technology Facilities Council (STFC) research grant to University College London (UCL), a SAO fellowship to Harvard-Smithsonian Center for Astrophysics and by European Space Agency (ESA) contract no. 4000120752/17/NL/MH. L. L. was supported by CNRS/INSU. C. L. was funded by CNES. E. J. B. was supported by STFC grant ST/N000749/1 and a Royal Society Wolfson Research Merit Award. L. C. R. was funded by an STFC consolidated grant to Lancaster University (ST/R000816/1). C. M. J.'s work at Southampton is supported by STFC Ernest Rutherford Fellowship ST/L004399/1. C. M. J.'s work at DIAS is supported by Science Foundation Ireland grant 18/FRL/6199. Z. H. Y. acknowledges financial support from the Belgian Federal Science Policy Office (BELSPO) via the PRODEX Programme of ESA. New Horizons SWAP data are available on the NASA Planetary Data System (PDS): https://pds-ppi.igpp.ucla.edu/search/?sc=New_Horizons&t=Jupiter&i=SWAP. The authors acknowledge the NDA team (at the Nançay Radio Observatory and LESIA, Observatoire de Paris) and the Wind/Waves team (at Goddard and LESIA, Observatoire de Paris) for providing access to radio data and the ExPRES team (at LESIA, Observatoire de Paris with support from Paris Astronomical Data Centre) for providing access to radio simulations. The NDA data were directly retrieved online at http://www.obs-nancay.fr, the ExPRES simulations at http://maser.obspm.fr/data/expres, and the Wind/Waves data from the CDAweb service at http://cdaweb.gsfc.nasa.gov. We also greatly thank the Chandra and XMM-Newton Projects for their support. The Jupiter X-ray observations presented here are publicly available on the Chandra archive (https://cda.harvard.edu/chaser/) and the XMM-Newton archive (http://nxsa.esac.esa.int/nxsa-web/#search), respectively. The mSWiM solar wind propagation model is publicly available from http://mswim.engin.umich.edu/. Tao model propagated solar wind data are available upon a request to C. T. (chihiro.tao@nict.go.jp) and publicly available at the AMDA database (http://amda.cdpp.eu). The Jupiter UV observations presented here are publicly available on the ESA Hubble archive: http://hst.esac.esa.int/ehst.

References

Badman, S., Bonfond, B., Fujimoto, M., Gray, R., Kasaba, Y., Kasahara, S., et al. (2016). Weakening of jupiter's main auroral emission during january 2014. *Geophysical Research Letters*, *43*, 988–997. https://doi.org/10.1002/2015GL067366

Badman, S. V., Branduardi-Raymont, G., Galand, M., Hess, S. L., Krupp, N., Lamy, L., et al. (2015). Auroral processes at the giant planets: Energy deposition, emission mechanisms, morphology and spectra. *Space Science Reviews*, *187*(1-4), 99–179.

Bagenal, F., Adriani, A., Allegrini, F., Bolton, S., Bonfond, B., Bunce, E., et al. (2014). Magnetospheric science objectives of the Juno mission. *Space Science Reviews*, *213*, 1–69.

Bagenal, F., Horányi, M., McComas, D. J., McNutt, R. L., Elliott, H. A., Hill, M. E., et al. (2016). Pluto's interaction with its space environment: Solar wind, energetic particles, and dust. *Science*, *351*(6279), aad9045.

Baron, R., Owen, T., Connerney, J., Satoh, T., & Harrington, J. (1996). Solar wind control of jupiter's H_3^+ auroras. *Icarus*, *120*(2), 437–442.

Bhattacharyya, D., Clarke, J. T., Montgomery, J., Bonfond, B., Gérard, J.-C., & Grodent, D. (2018). Evidence for auroral emissions from Callisto's footprint in HST UV images. *Journal of Geophysical Research: Space Physics*, *123*, 364–373. https://doi.org/10.1002/2017JA024791

Boischot, A., Rosolen, C., Aubier, M., Daigne, G., Genova, F., Leblanc, Y., et al. (1980). A new high-grain, broadband, steerable array to study Jovian decametric emission. *Icarus*, *43*(3), 399–407.

Bonfond, B., Gladstone, G., Grodent, D., Greathouse, T., Versteeg, M., Hue, V., et al. (2017). Morphology of the UV aurorae Jupiter during Juno's first perijove observations. *Geophysical Research Letters*, *44*, 4463–4471. https://doi.org/10.1002/2017GL073114

Bonfond, B., Grodent, D., Badman, S. V., Gérard, J.-C., & Radioti, A. (2016). Dynamics of the flares in the active polar region of Jupiter. *Geophysical Research Letters*, *43*, 11,963–11,970. https://doi.org/10.1002/2016GL071757

Bonfond, B., Grodent, D., Gérard, J.-C., Radioti, A., Dols, V., Delamere, P., & Clarke, J. (2009). The Io UV footprint: Location, inter-spot distances and tail vertical extent. *Journal of Geophysical Research*, *114*, A07224. https://doi.org/10.1029/2009JA014312

Bonfond, B., Hess, S., Bagenal, F., Gérard, J.-C., Grodent, D., Radioti, A., et al. (2013). The multiple spots of the ganymede auroral footprint. *Geophysical Research Letters*, *40*, 4977–4981. https://doi.org/10.1002/grl.50989

Bonfond, B., Vogt, M., Gérard, J.-C., Grodent, D., Radioti, A., & Coumans, V. (2011). Quasi-periodic polar flares at Jupiter: A signature of pulsed dayside reconnections? *Geophysical Research Letters*, *38*, L02104. https://doi.org/10.1029/2010GL045981

Bougeret, J.-L., Kaiser, M. L., Kellogg, P., Manning, R., Goetz, K., Monson, S., et al. (1995). Waves: The radio and plasma wave investigation on the wind spacecraft. *Space Science Reviews*, *71*(1-4), 231–263.

Branduardi-Raymont, G., Bhardwaj, A., Elsner, R., Gladstone, G., Ramsay, G., Rodriguez, P., et al. (2007). A study of Jupiter's aurorae with XMM-Newton. *Astronomy & Astrophysics*, *463*(2), 761–774.

Branduardi-Raymont, G., Elsner, R. F., Galand, M., Grodent, D., Cravens, T., Ford, P., et al. (2008). Spectral morphology of the X-ray emission from Jupiter's aurorae. *Journal of Geophysical Research*, *113*, A02202. https://doi.org/10.1029/2007JA012600

Branduardi-Raymont, G., Elsner, R., Gladstone, G., Ramsay, G., Rodriguez, P., Soria, R., & Waite, J. Jr. (2004). First observation of Jupiter by XMM-Newton. *Astronomy & Astrophysics*, *424*(1), 331–337.

Bunce, E., Cowley, S., & Yeoman, T. (2004). Jovian cusp processes: Implications for the polar aurora. *Journal of Geophysical Research*, *109*, A09S13. https://doi.org/10.1029/2003JA010280

Chané, E., Saur, J., Keppens, R., & Poedts, S. (2017). How is the Jovian main auroral emission affected by the solar wind? *Journal of Geophysical Research: Space Physics*, *122*, 1960–1978. https://doi.org/10.1002/2016JA023318

Clark, G., Mauk, B., Haggerty, D., Paranicas, C., Kollmann, P., Rymer, A., et al. (2017). Energetic particle signatures of magnetic field-aligned potentials over Jupiter's polar regions. *Geophysical Research Letters*, *44*, 8703–8711. https://doi.org/10.1002/2017GL074366

Clarke, J., Nichols, J., Gérard, J.-C., Grodent, D., Hansen, K., Kurth, W., et al. (2009). Response of Jupiter's and Saturn's auroral activity to the solar wind. *Journal of Geophysical Research*, *114*, A05210. https://doi.org/10.1029/2008JA013694

Connerney, J., Acuna, M., Ness, N., & Satoh, T. (1998). New models of Jupiter's magnetic field constrained by the Io flux tube footprint. *Journal of Geophysical Research*, *103*(A6), 11,929–11,939.

Cowley, S. (2006). Current-voltage and kinetic energy flux relations for relativistic field-aligned acceleration of auroral electrons. *Annales Geophysicae*, *24*, 325–338.

Cowley, S., Badman, S. V., Imber, S., & Milan, S. (2008). Comment on Jupiter: A fundamentally different magnetospheric interaction with the solar wind? by DJ McComas and F. Bagenal. *Geophysical Research Letters*, *35*, L10101. https://doi.org/10.1029/2007GL032645

Cowley, S., & Bunce, E. (2001). Origin of the main auroral oval in Jupiter's coupled magnetosphere–ionosphere system. *Planetary and Space Science*, *49*(10), 1067–1088.

Cowley, S., & Bunce, E. (2003a). Modulation of Jupiter's main auroral oval emissions by solar wind induced expansions and compressions of the magnetosphere. *Planetary and Space Science*, *51*(1), 57–79.

Cowley, S., & Bunce, E. (2003b). Modulation of Jovian middle magnetosphere currents and auroral precipitation by solar wind-induced compressions and expansions of the magnetosphere: Initial response and steady state. *Planetary and Space Science*, *51*(1), 31–56.

Cowley, S., Bunce, E., Stallard, T., & Miller, S. (2003). Jupiter's polar ionospheric flows: Theoretical interpretation. *Geophysical Research Letters*, *30*(5), 1220. https://doi.org/10.1029/2002GL016030

Cowley, S., Nichols, J., & Andrews, D. (2007). Modulation of Jupiter's plasma flow, polar currents, and auroral precipitation by solar wind-induced compressions and expansions of the magnetosphere: A simple theoretical model. *Annales Geophysicae*, *25*, 1433–1463.

Cravens, T., Howell, E., Waite, J., & Gladstone, G. (1995). Auroral oxygen precipitation at Jupiter. *Journal of Geophysical Research*, *100*(A9), 17,153–17,161.

Cravens, T., Waite, J., Gombosi, T., Lugaz, N., Gladstone, G., Mauk, B., & MacDowall, R. (2003). Implications of Jovian X-ray emission for magnetosphere-ionosphere coupling. *Journal of Geophysical Research*, *108*(A12), 1465. https://doi.org/10.1029/2003JA010050

Delamere, P., & Bagenal, F. (2010). Solar wind interaction with Jupiter's magnetosphere. *Journal of Geophysical Research*, *115*, A10201. https://doi.org/10.1029/2010JA015347

Desch, M., & Barrow, C. (1984). Direct evidence for solar wind control of Jupiter's hectometer-wavelength radio emission. *Journal of Geophysical Research*, *89*(A8), 6819–6823.

Dunn, W. R., Branduardi-Raymont, G., Carter-Cortez, V., Campbell, A., Elsner, R. F., Ness, J.-U., et al. (2020). Jupiter's X-ray emission during the 2007 solar minimum. *Journal of Geophysical Research: Space Physics*, *125*, e2019JA027219. https://doi.org/10.1029/2019JA027219

Dunn, W. R., Branduardi-Raymont, G., Elsner, R. F., Vogt, M. F., Lamy, L., Ford, P. G., et al. (2016). The impact of an ICME on the Jovian X-ray aurora. *Journal of Geophysical Research: Space Physics*, *121*, 2274–2307. https://doi.org/10.1002/2015JA021888

Dunn, W., Branduardi-Raymont, G., Ray, L., Jackman, C., Kraft, R., Elsner, R., et al. (2017). The independent pulsations of Jupiter's northern and southern X-ray auroras. *Nature Astronomy*, *1*(11), 758.

Ebert, R. W., Bagenal, F., McComas, D. J., & Fowler, C. M. (2014). A survey of solar wind conditions at 5 AU: A tool for interpreting solar wind-magnetosphere interactions at Jupiter. *Frontiers in Astronomy and Space Sciences*, *1*, 4.

Ebert, R., McComas, D., Bagenal, F., & Elliott, H. (2010). Location, structure, and motion of Jupiter's dusk magnetospheric boundary from 1625 to 2550 R_J. *Journal of Geophysical Research*, *115*, A12223. https://doi.org/10.1029/2010JA015938

Echer, E., Zarka, P., Gonzalez, W., Morioka, A., & Denis, L. (2010). Solar wind effects on jupiter non-Io dam emissions during Ulysses distant encounter (2003–2004). *Astronomy & Astrophysics*, *519*, A84.

Elliott, H., McComas, D., Valek, P., Nicolaou, G., Weidner, S., & Livadiotis, G. (2016). The new Horizons solar wind around Pluto (SWAP) observations of the solar wind from 11–33 AU. *The Astrophysical Journal Supplement Series*, *223*(2), 19.

Elliott, H. A., McComas, D. J., Zirnstein, E. J., Randol, B. M., Delamere, P. A., Livadiotis, G., et al. (2019). Slowing of the solar wind in the outer heliosphere. *The Astrophysical Journal*, *885*(2), 156.

Elliott, H., Valek, P., McComas, D., Delamere, P., Bagenal, F., Gladstone, G., et al. (2018). Determining the alpha to proton density ratio for the new horizons solar wind observations. *The Astrophysical Journal*, *866*(2), 85.

Elsner, R. F., Lugaz, N., Waite, J., Cravens, T., Gladstone, G., Ford, P., et al. (2005). Simultaneous Chandra X ray, Hubble Space Telescope ultraviolet, and Ulysses radio observations of Jupiter's aurora. *Journal of Geophysical Research*, *110*, A01207. https://doi.org/10.1029/2004JA010717

Forsyth, C., Fazakerley, A., Rae, I., Watt, C., Murphy, K., Wild, J. A., et al. (2014). In situ spatiotemporal measurements of the detailed azimuthal substructure of the substorm current wedge. *Journal of Geophysical Research: Space Physics*, *119*, 927–946. https://doi.org/10.1002/2013JA019302

Gladstone, G., Waite, J., Grodent, D., Lewis, W., Crary, F., Elsner, R. F., et al. (2002). A pulsating auroral X-ray hot spot on Jupiter. *Nature*, *415*(6875), 1000–1003.

Gray, R., Badman, S. V., Bonfond, B., Kimura, T., Misawa, H., Nichols, J., et al. (2016). Auroral evidence of radial transport at Jupiter during January 2014. *Journal of Geophysical Research: Space Physics*, *121*, 9972–9984. https://doi.org/10.1002/2016JA023007

Grodent, D. (2015). A brief review of ultraviolet auroral emissions on giant planets. *Space Science Reviews*, *187*(1-4), 23–50.

Grodent, D., Bonfond, B., Gérard, J.-C., Radioti, A., Gustin, J., Clarke, J. T., et al. (2008). Auroral evidence of a localized magnetic anomaly in Jupiter's northern hemisphere. *Journal of Geophysical Research*, *113*, A09201. https://doi.org/10.1029/2008JA013185

Grodent, D., Bonfond, B., Yao, Z., Gérard, J.-C., Radioti, A., Dumont, M., et al. (2018). Jupiter's aurora observed with HST during Juno orbits 3 to 7. *Journal of Geophysical Research: Space Physics*, *123*, 3299–3319. https://doi.org/10.1002/2017JA025046

Guo, R., Yao, Z., Sergis, N., Wei, Y., Mitchell, D., Roussos, E., et al. (2018). Reconnection acceleration in Saturn's dayside magnetodisk: A multicase study with Cassini. *The Astrophysical Journal Letters*, *868*(2), L23.

Guo, R., Yao, Z., Wei, Y., Ray, L. C., Rae, I., Arridge, C. S., et al. (2018). Rotationally driven magnetic reconnection in Saturn's dayside. *Nature Astronomy*, *1*, 640–645.

Gurnett, D., Kurth, W., Hospodarsky, G., Persoon, A., Zarka, P., Lecacheux, A., et al. (2002). Control of Jupiter's radio emission and aurorae by the solar wind. *Nature*, *415*(6875), 985–987.

Gustin, J., Bonfond, B., Grodent, D., & Gérard, J.-C. (2012). Conversion from HST ACS and STIS auroral counts into brightness, precipitated power, and radiated power for H_2 giant planets. *Journal of Geophysical Research*, *117*, A07316. https://doi.org/10.1029/2012JA017607

Hess, S., Cecconi, B., & Zarka, P. (2008). Modeling of Io-Jupiter decameter arcs, emission beaming and energy source. *Geophysical Research Letters*, *35*, L13107. https://doi.org/10.1029/2008GL033656

Hess, S. L., Delamere, P., Dols, V., Bonfond, B., & Swift, D. (2010). Power transmission and particle acceleration along the Io flux tube. *Journal of Geophysical Research*, *115*, A06205. https://doi.org/10.1029/2009JA014928

Hess, S., Delamere, P., Dols, V., & Ray, L. (2011). Comparative study of the power transferred from satellite-magnetosphere interactions to auroral emissions. *Journal of Geophysical Research*, *116*, A01202. https://doi.org/10.1029/2010JA015807

Hess, S., Echer, E., & Zarka, P. (2012). Solar wind pressure effects on Jupiter decametric radio emissions independent of Io. *Planetary and Space Science*, *70*(1), 114–125.

Hess, S., Echer, E., Zarka, P., Lamy, L., & Delamere, P. (2014). Multi-instrument study of the Jovian radio emissions triggered by solar wind shocks and inferred magnetospheric subcorotation rates. *Planetary and Space Science*, *99*, 136–148.

Hill, T. (2001). The Jovian auroral oval. *Journal of Geophysical Research*, *106*(A5), 8101–8107.

Houston, S., Cravens, T. E., Schultz, D. R., Gharibnejad, H., Dunn, W. R., Haggerty, D. K., et al. (2020). Jovian auroral ion precipitation: X-ray production from oxygen and sulfur precipitation. *Journal of Geophysical Research: Space Physics*, *125*, e2019JA027007. https://doi.org/10.1029/2019JA027007

Houston, S., Ozak, N., Young, J., Cravens, T., & Schultz, D. (2018). Jovian auroral ion precipitation: Field-aligned currents and ultraviolet emissions. *Journal of Geophysical Research: Space Physics*, *123*, 2257–2273. https://doi.org/10.1002/2017JA024872

Jackman, C., Knigge, C., Altamirano, D., Gladstone, R., Dunn, W., Elsner, R., et al. (2018). Assessing quasi-periodicities in Jovian X-ray emissions: Techniques and heritage survey. *Journal of Geophysical Research: Space Physics*, *123*, 9204–9221. https://doi.org/10.1029/2018JA025490

Jia, X., Kivelson, M. G., Khurana, K. K., & Walker, R. J. (2010). Magnetic fields of the satellites of Jupiter and Saturn. *Space Science Reviews*, *152*(1-4), 271–305.

Joy, S., Kivelson, M., Walker, R., Khurana, K., Russell, C., & Ogino, T. (2002). Probabilistic models of the Jovian magnetopause and bow shock locations. *Journal of Geophysical Research*, *107*(A10), 1309. https://doi.org/10.1029/2001JA009146

Kimura, T., Badman, S., Tao, C., Yoshioka, K., Murakami, G., Yamazaki, A., et al. (2015). Transient internally driven aurora at Jupiter discovered by Hisaki and the Hubble Space Telescope. *Geophysical Research Letters*, *42*, 1662–1668. https://doi.org/10.1002/2015GL063272

Kimura, T., Kraft, R., Elsner, R., Branduardi-Raymont, G., Gladstone, G., Tao, C., et al. (2016). Jupiter's X-ray and EUV auroras monitored by Chandra, XMM-Newton, and Hisaki satellite. *Journal of Geophysical Research: Space Physics*, *121*, 2308–2320. https://doi.org/10.1002/2015JA021893

Kita, H., Kimura, T., Tao, C., Tsuchiya, F., Misawa, H., Sakanoi, T., et al. (2016). Characteristics of solar wind control on Jovian UV auroral activity deciphered by long-term Hisaki exceed observations: Evidence of preconditioning of the magnetosphere? *Geophysical Research Letters*, *43*, 6790–6798. https://doi.org/10.1002/2016GL069481

Kivelson, M. G. (2004). Moon–magnetosphere interactions: A tutorial. *Advances in Space Research*, *33*(11), 2061–2077.

Lamy, L., Zarka, P., Cecconi, B., Klein, L., Masson, S., Denis, L., et al. (2017). 1977-2017: 40 years of decametric observations of Jupiter and the sun with the Nançay decameter array. *Planetary Radio Emissions VIII*, 455–466.

Lamy, L., Prangé, R., Hansen, K., Clarke, J., Zarka, P., Cecconi, B., et al. (2012). Earth-based detection of Uranus' aurorae. *Geophysical Research Letters*, *39*, L07105. https://doi.org/10.1029/2012GL051312

Leahy, D., Darbro, W., Elsner, R., Weisskopf, M., Kahn, S., Sutherland, P., & Grindlay, J. (1983). On searches for pulsed emission with application to four globular cluster X-ray sources-NGC 1851, 6441, 6624, and 6712. *The Astrophysical Journal*, *266*, 160–170.

Lecacheux, A. (2000). The Nançay decameter array: A useful step towards giant, new generation radio telescopes for long wavelength radio astronomy. *Radio Astronomy at Long Wavelengths*, *119*, 321–328.

Louis, C. K., Hess, S. L. G., Cecconi, B., Zarka, P., Lamy, L., Aicardi, S., & Loh, A. (2019). ExPRES: An exoplanetary and planetary radio emissions simulator. *Astronomy & Astrophysics*, *627*, A30. https://doi.org/10.1051/0004-6361/201935161

Louis, C., Lamy, L., Zarka, P., Cecconi, B., Imai, M., Kurth, W., et al. (2017). Io-Jupiter decametric arcs observed by Juno/Waves compared to ExPRES simulations. *Geophysical Research Letters*, *44*, 9225–9232. https://doi.org/10.1002/2017GL073036

Ma, X., Delamere, P., Otto, A., & Burkholder, B. (2017). Plasma transport driven by the three-dimensional Kelvin-Helmholtz instability. *Journal of Geophysical Research: Space Physics*, *122*, 10,382–10,395. https://doi.org/10.1002/2017JA024394

MacDowall, R., Kaiser, M., Desch, M., Farrell, W., Hess, R., & Stone, R. (1993). Quasiperiodic Jovian radio bursts: Observations from the Ulysses radio and plasma wave experiment. *Planetary and Space Science*, *41*(11), 1059–1072.

Manners, H., Masters, A., & Yates, J. (2018). Standing Alfvén waves in Jupiter's magnetosphere as a source of 10- to 60-min quasiperiodic pulsations. *Geophysical Research Letters*, *45*, 8746–8754. https://doi.org/10.1029/2018GL078891

Marques, M., Zarka, P., Echer, E., Ryabov, V., Alves, M., Denis, L., & Coffre, A. (2017). Statistical analysis of 26 yr of observations of decametric radio emissions from Jupiter. *Astronomy & Astrophysics*, *604*, A17.

Mauk, B., Clarke, J., Grodent, D., Waite, J., Paranicas, C., & Williams, D. (2002). Transient aurora on Jupiter from injections of magnetospheric electrons. *Nature*, *415*(6875), 1003–1005.

Mauk, B., Haggerty, D., Paranicas, C., Clark, G., Kollmann, P., Rymer, A., et al. (2017). Juno observations of energetic charged particles over Jupiter's polar regions: Analysis of monodirectional and bidirectional electron beams. *Geophysical Research Letters*, *44*, 4410–4418. https://doi.org/10.1002/2016GL072286

Mauk, B. H., & Saur, J. (2007). Equatorial electron beams and auroral structuring at Jupiter. *Journal of Geophysical Research*, *112*, A10221. https://doi.org/10.1029/2007JA012370

McComas, D., Allegrini, F., Bagenal, F., Casey, P., Delamere, P., Demkee, D., et al. (2008). The solar wind around Pluto (SWAP) instrument aboard new horizons. *Space Science Reviews*, *140*(1-4), 261–313.

McComas, D., Allegrini, F., Bagenal, F., Crary, F., Ebert, R., Elliott, H., et al. (2007). Diverse plasma populations and structures in Jupiter's magnetotail. *Science*, *318*(5848), 217–220.

McComas, D., & Bagenal, F. (2007). Jupiter: A fundamentally different magnetospheric interaction with the solar wind. *Geophysical Research Letters*, *34*, L10103. https://doi.org/10.1029/2008GL034351

McComas, D., Elliott, H., Weidner, S., Valek, P., Zirnstein, E., Bagenal, F., et al. (2016). Pluto's interaction with the solar wind. *Journal of Geophysical Research: Space Physics*, *121*, 4232–4246. https://doi.org/10.1002/2016JA022599

Nichols, J., Badman, S. V., Bagenal, F., Bolton, S., Bonfond, B., Bunce, E., et al. (2017). Response of Jupiter's auroras to conditions in the interplanetary medium as measured by the Hubble Space Telescope and Juno. *Geophysical Research Letters*, *44*, 7643–7652. https://doi.org/10.1002/2017GL073029

Nichols, J., Clarke, J., Gérard, J.-C., & Grodent, D. (2009a). Observations of Jovian polar auroral filaments. *Geophysical Research Letters*, *36*, L08101. https://doi.org/10.1029/2009GL037578

Nichols, J., Clarke, J., Gérard, J.-C., Grodent, D., & Hansen, K. (2009b). Variation of different components of Jupiter's auroral emission. *Journal of Geophysical Research*, *114*, A06210. https://doi.org/10.1029/2009JA014051

Nichols, J., Yeoman, T., Bunce, E., Chowdhury, M., Cowley, S., & Robinson, T. (2017). Periodic emission within Jupiter's main auroral oval. *Geophysical Research Letters*, *44*, 9192–9198. https://doi.org/10.1002/2017GL074824

Nicolaou, G., McComas, D., Bagenal, F., & Elliott, H. (2014). Properties of plasma ions in the distant Jovian magnetosheath using solar wind around pluto data on new horizons. *Journal of Geophysical Research: Space Physics*, *119*, 3463–3479. https://doi.org/10.1002/2013JA019665

Nicolaou, G., McComas, D., Bagenal, F., Elliott, H., & Ebert, R. (2015). Jupiter's deep magnetotail boundary layer. *Planetary and Space Science*, *111*, 116–125.

Owens, M. J., & Forsyth, R. J. (2013). The heliospheric magnetic field. *Living Reviews in Solar Physics*, *10*(1), 5.

Pallier, L., & Prangé, R. (2001). More about the structure of the high latitude Jovian aurorae. *Planetary and Space Science*, *49*(10), 1159–1173.

Pallier, L., & Prangé, R. (2004). Detection of the southern counterpart of the Jovian northern polar cusp: Shared properties. *Geophysical Research Letters*, *31*, L06701. https://doi.org/10.1029/2003GL018041

Paranicas, C., Mauk, B., Haggerty, D., Clark, G., Kollmann, P., Rymer, A., et al. (2018). Intervals of intense energetic electron beams over Jupiter's poles. *Journal of Geophysical Research: Space Physics*, *123*, 1989–1999. https://doi.org/10.1002/2017JA025106

Prangé, R., Pallier, L., Hansen, K. C., Howard, R., Vourlidas, A., Courtin, R., & Parkinson, C. (2004). An interplanetary shock traced by planetary auroral storms from the Sun to Saturn. *Nature*, *432*(7013), 78–81.

Prangé, R., Zarka, P., Ballester, G., Livengood, T., Denis, L., Carr, T., et al. (1993). Correlated variations of UV and radio emissions during an outstanding Jovian auroral event. *Journal of Geophysical Research*, *98*(E10), 18,779–18,791.

Radioti, A., Grodent, D., Gérard, J.-C., Vogt, M., Lystrup, M., & Bonfond, B. (2011). Nightside reconnection at Jupiter: Auroral and magnetic field observations from 26 July 1998. *Journal of Geophysical Research*, *116*, A03221. https://doi.org/10.1029/2010JA016200

Saur, J., Neubauer, F. M., Connerney, J., Zarka, P., & Kivelson, M. G. (2004). Plasma interaction of Io with its plasma torus, Jupiter: The planet. *Satellites and Magnetosphere*, *1*, 537–560.

Shi, Q., Hartinger, M., Angelopoulos, V., Tian, A., Fu, S., Zong, Q.-G., et al. (2014). Solar wind pressure pulse-driven magnetospheric vortices and their global consequences. *Journal of Geophysical Research: Space Physics*, *119*, 4274–4280. https://doi.org/10.1002/2013JA019551

Sinclair, J., Orton, G., Fernandes, J., Kasaba, Y., Sato, T., Fujiyoshi, T., et al. (2019). A brightening of Jupiter's auroral 7.8-μm CH 4 emission during a solar-wind compression. *Nature Astronomy*, *3*, 607–613.

Smith, R., Foster, A., & Brickhouse, N. (2012). Approximating the X-ray spectrum emitted from astrophysical charge exchange. *Astronomische Nachrichten*, *333*(4), 301–304.

Southwood, D., & Kivelson, M. (2001). A new perspective concerning the influence of the solar wind on the Jovian magnetosphere. *Journal of Geophysical Research*, *106*(A4), 6123–6130.

Stallard, T. S., Clarke, J. T., Melin, H., Miller, S., Nichols, J. D., O'Donoghue, J., et al. (2016). Stability within Jupiter's polar auroral swirl region over moderate timescales. *Icarus*, *268*, 145–155.

Stallard, T., Miller, S., Cowley, S., & Bunce, E. (2003). Jupiter's polar ionospheric flows: Measured intensity and velocity variations poleward of the main auroral oval. *Geophysical Research Letters*, *30*(5), 1221. https://doi.org/10.1029/2002GL016031

Szalay, J., Bonfond, B., Allegrini, F., Bagenal, F., Bolton, S., Clark, G., et al. (2018). In situ observations connected to the Io footprint tail aurora. *Journal of Geophysical Research: Planets*, *123*, 3061–3077. https://doi.org/10.1029/2018JE005752

Tao, C., Kataoka, R., Fukunishi, H., Takahashi, Y., & Yokoyama, T. (2005). Magnetic field variations in the Jovian magnetotail induced by solar wind dynamic pressure enhancements. *Journal of Geophysical Research*, *110*, A11208. https://doi.org/10.1029/2004JA010959

Vogt, M. F., Bunce, E. J., Kivelson, M. G., Khurana, K. K., Walker, R. J., Radioti, A., et al. (2015). Magnetosphere-ionosphere mapping at Jupiter: Quantifying the effects of using different internal field models. *Journal of Geophysical Research : Space Physics*, *120*, 2584–2599. https://doi.org/10.1002/2014JA020729

Von Steiger, R., Schwadron, N., Fisk, L., Geiss, J., Gloeckler, G., Hefti, S., et al. (2000). Composition of quasi-stationary solar wind flows from Ulysses/solar wind ion composition spectrometer. *Journal of Geophysical Research*, *105*(A12), 27,217–27,238.

Watanabe, H., Kita, H., Tao, C., Kagitani, M., Sakanoi, T., & Kasaba, Y. (2018). Pulsation characteristics of Jovian infrared northern aurora observed by the Subaru IRCS with adaptive optics. *Geophysical Research Letters*, *45*, 11,547–11,554. https://doi.org/10.1029/2018GL079411

Yao, Z., Coates, A., Ray, L., Rae, I., Grodent, D., Jones, G. H., et al. (2017). Corotating magnetic reconnection site in Saturn's magnetosphere. *The Astrophysical Journal Letters*, *846*(2), L25.

Yates, J., Achilleos, N., & Guio, P. (2014). Response of the Jovian thermosphere to a transient "pulse" in solar wind pressure. *Planetary and Space Science*, *91*, 27–44.

Zarka, P. (1998). Auroral radio emissions at the outer planets: Observations and theories. *Journal of Geophysical Research*, *103*(E9), 20,159–20,194.

Zhao, H., Shen, X., Tang, B., Tian, A., Shi, Q., Weygand, J., et al. (2016). Magnetospheric vortices and their global effect after a solar wind dynamic pressure decrease. *Journal of Geophysical Research: Space Physics*, *121*, 1071–1077. https://doi.org/10.1002/2015JA021646

Zieger, B., & Hansen, K. C. (2008). Statistical validation of a solar wind propagation model from 1 to 10 AU. *Journal of Geophysical Research*, *113*, A08107. https://doi.org/10.1029/2008JA013046